



**HAL**  
open science

## Dynamics of a Newtonian droplet in the turbulent flow of a shear thinning fluid in a micro-channel

Yongbin Ji, Elia Missi, Jérôme Bellettre, Teodor Burghilea, Agnès Montillet, Patrizio Massoli

► **To cite this version:**

Yongbin Ji, Elia Missi, Jérôme Bellettre, Teodor Burghilea, Agnès Montillet, et al.. Dynamics of a Newtonian droplet in the turbulent flow of a shear thinning fluid in a micro-channel. *Physical Review Fluids*, 2023, 8 (4), pp.043301. 10.1103/PhysRevFluids.8.043301 . hal-04005170

**HAL Id: hal-04005170**

**<https://hal.science/hal-04005170>**

Submitted on 26 Feb 2023

**HAL** is a multi-disciplinary open access archive for the deposit and dissemination of scientific research documents, whether they are published or not. The documents may come from teaching and research institutions in France or abroad, or from public or private research centers.

L'archive ouverte pluridisciplinaire **HAL**, est destinée au dépôt et à la diffusion de documents scientifiques de niveau recherche, publiés ou non, émanant des établissements d'enseignement et de recherche français ou étrangers, des laboratoires publics ou privés.

# Dynamics of a Newtonian droplet in the turbulent flow of a shear thinning fluid in a micro-channel

Yongbin Ji\*

*Department of Mechanical and Automation Engineering,  
The Chinese University of Hong Kong, Hong Kong SAR, China<sup>†</sup>*

Elia Missi<sup>‡</sup>

*LTeN UMR CNRS 6607, Nantes Université ,  
1 rue Christian Pauc, CS 50609, 44306 Nantes Cedex 3, France*

Jérôme Bellettre<sup>§</sup>

*LTeN UMR CNRS 6607, Nantes Université ,  
1 rue Christian Pauc, CS 50609, 44306 Nantes Cedex 3, France*

Agnès Montillet<sup>¶</sup>

*Nantes Université , Oniris, CNRS, GEPEA,  
UMR 6144, F-44600 Saint-Nazaire, France*

Patrizio Massoli<sup>\*\*</sup>

*Institute of Sciences and Technologies for Sustainable Energy and  
Mobility (STEMS) - CNR, Viale Marconi 4, 80125 Napoli, Italy*

Teodor Burghelea<sup>††</sup>

*LTeN UMR CNRS 6607, Nantes Université ,  
1 rue Christian Pauc, CS 50609, 44306 Nantes Cedex 3, France*

(Dated:)

A systematic experimental investigation of the dynamics of a Newtonian drop in microscopic cross-slot of a shear thinning and inelastic fluid (aqueous solutions of xanthan) is presented. The flows are driven at large Reynolds numbers and are relevant to efficient high-throughput emulsification in micro-channels. Depending on the initial size of the drop, the driving flow rates and the rheological behaviour of the continuous phase, two fundamental dynamic modes are observed. The first dynamic mode relates to the trapping of the drop. By time-resolved tracking of both the positions and the deformations of the drop over 100 distinct drops a comprehensive statistical description of the trapping events is provided. The probability of trapping when xanthan solutions are used as a continuous phase follow a common trend when the effective strength of the swirling flow motion within the impingement region is gradually increased by tuning both the flow rates and the polymer concentration suggesting that the trapping events emerge via an imperfect bifurcation. A second phenomenon that is of particular relevance to the emulsification process relates to the breakup of drops. The dynamics of the breakup process are quantitatively described in terms of the characteristic breakup times, number of emerging daughter droplets and drop morphology are equally dependent on both the driving flow rates and the polymer concentration. Further physical insights into the intricate coupling between the flow conditions, the shear thinning rheology of the continuous phase and the single drop dynamics are obtained in terms of a quantitative description of the kinematics of drop deformation. This analysis was performed using a novel tool that allows one to assess the velocity distributions along the drop contours and extract the rates of deformation, the strains corresponding to the breakup process and the kinematic print of the flow (shear or extension). Finally, a full diagram mapping all the **modes of the single droplet dynamics** is presented.

---

\* [yongbinji@cuhk.edu.hk](mailto:yongbinji@cuhk.edu.hk)

† LTeN UMR CNRS 6607, Nantes Université , 1 rue Christian Pauc, CS 50609, 44306 Nantes Cedex 3, France

‡ [Elia.Missi@univ-nantes.fr](mailto:Elia.Missi@univ-nantes.fr)

§ [jerome.bellettre@univ-nantes.fr](mailto:jerome.bellettre@univ-nantes.fr)

¶ [Agnes.Montillet@univ-nantes.fr](mailto:Agnes.Montillet@univ-nantes.fr)

\*\* [patrizio.massoli@stems.cnr.it](mailto:patrizio.massoli@stems.cnr.it)

†† [Teodor.Burghelea@univ-nantes.fr](mailto:Teodor.Burghelea@univ-nantes.fr)

**CONTENTS**

List of Figures	4
I. Introduction	7
II. Experimental methods	9
A. Choice and rheological characterization of the working fluids	9
1. Choice of working fluids	9
2. Rheological characterisation of the fluids	10
B. Experimental setup	13
1. Microscopic flow channel	13
2. Data acquisition system	14
C. Data analysis	15
III. Results	17
A. Summary of the experiments	17
B. Trapping and deformation dynamics of a single oil droplet for various xanthan concentrations in the continuous phase.	19
C. Breakup dynamics of a single oil droplet for various xanthan concentrations in the continuous phase	22
IV. Conclusions, outlook	29
V. Acknowledgements	33
References	33



## LIST OF FIGURES

- 1 Schematic representation of the high shear rate microfluidic rheometer:  $Q$  - flow rate of the fluid to be characterized,  $Q_R$  - flow rate of the reference fluid with a known viscosity,  $W$  - transverse extent of the fluid to be characterized,  $W_R$  - transverse extent of the reference fluid. .... 11
- 2 (a) Rheological flow curves measured for three distinct xanthan concentrations indicated in the insert via two alternative techniques (see text for description): classical rotational rheology - full symbols, microfluidic high shear rate rheology - open symbols. The full lines are nonlinear fitting functions obtained according to the Carreau-Yasuda model and the highlighted regions indicate the confidence interval of the fitting procedure. The stars and the dashed line mark the critical line  $(\dot{\gamma}_c, \eta_c)$  defined by the condition  $Re_c = 0.1$  that defines the inertia-free range of the classical rotational rheology measurements (see text for details/discussion). (b) Dependence of the zero shear viscosity  $\eta_0$  on the concentration of xanthan  $C_x$ . The lines are power law fitting functions (see text for description). The vertical arrows point the concentration bounds  $C^*, C^{**}$  of the relevant concentrated regimes. .... 12
- 3 (a) Schematic view of the microfluidic chip. (b) **Top:** Frontal (camera) view of the cross-slot region in the  $(x, y)$  plane. **Bottom:** Lateral view (not accessible through our measurements but only hinted as) of the cross-slot region in the  $(y, z)$  plane. The colors are as follows: blue and yellow regions refer to the channel inlets while the red highlighted region is the impingement zone. The "cartoon" arrow is solely a visual hint for the three dimensional flow structure dominated by the presence of a swirl located at the centre of the cross-slot region later referred to in the paper. .... 14
- 4 Schematic representation of the experimental system for the visualization of single drop dynamics: **IFC**<sub>1,2</sub> - input fluid containers, **OFC** - output fluid container, **DB**<sub>1,2</sub> - digital balances, **P**<sub>1,2</sub> - fluid pumps, **PT**<sub>1,2</sub> - pressure transducers, **PC**<sub>1,2</sub> - data acquisition computers, **MFC**- microfluidic chip, **HL** - halogen lamp, **CCD** - digital camera, **ZL** - zoom lens. .... 15
- 5 (a) Illustrations of the image processing sequence: **Top:** Original image **Middle:** Image after subtracting the background and enhancing the contrast **Bottom:** Binary closed image with the contours of the identified objects (droplets) superposed. (b) Illustration of the front tracking for a mother droplet in a water matrix and the flow rates  $50 - 6.3 \text{ mL/min}$ . The black full line represents the initial contour of the drop, the dashed red its final contour. The black circle is the initial centroid of the drop while the red square is its final centroid. The color map of the velocity vectors relates to their magnitude (red - small values, blue - large values). .... 16
- 6 Illustrations of single droplet dynamics for several xanthan concentrations indicated in the top inserts and flow rates are  $50 - 6.3 \text{ mL/min}$ . The scatter refers to the instantaneous positions of the centre of mass of the oil droplet. Both the false color and the relative size of the symbols map the deformation parameter  $DP$ . In each panel the red highlighted zone marks the impingement region. .... 19

- 7 (a) Time series of the deformation parameter  $DP$  corresponding to the data illustrated in Fig. 6. The time axis is normalized by the residence time  $t_r$  of the drop in the field of view. (b) Probability density functions corresponding to the time series illustrated in panel 7(a). (c) Summary of the trapping statistics: bottom-left axis - dependence of the trapping time  $t_{trapping}$  on the concentration of xanthan in the continuous phase, bottom -right - dependence of the time averaged deformation parameter  $\langle DP \rangle_t$  on the xanthan concentration. (d) Probability density functions of the in plane velocity of an oil droplet exhibiting trapping behaviour for three concentrations  $C_x$  of xanthan in the continuous phase indicated in the top inserts. . . . . 21
- 8 (a) Probability of trapping of a single oil drop as a function of the concentration  $C_x$  of xanthan in the continuous phase for several combinations of flow rates indicated in the legend. The full lines are cubic spline interpolating functions that solely serve as a guide for the eye. (b) Dependence of the trapping probability  $P_t$  on the effective swirl efficiency  $\Psi_{eff}$ . The full line is a guide for the eye,  $P_t \propto (\Psi_{eff} - 0.1)^{0.5}$ . (c) Dependence of the averaged (over 100 individual events) breakup times of the single oil droplet for various flow rates indicated in the insert on the volume fraction of xanthan in the continuous phase. The full lines are cubic spline interpolating functions that solely serve as a guide for the eye. . . . . 23
- 9 Illustration of the dynamics of droplet breakup for several xanthan concentrations in the continuous phase and the flow rates  $50 - 6.3mL/min$ : (a)  $C_x = 0\%$ , (b)  $C_x = 0.05\%$ , (c)  $C_x = 0.1\%$ , (d)  $C_x = 0.15\%$ , (e)  $C_x = 0.2\%$ . In each sub-panel the red contours delineate the oil-water interface. . . . . 24
- 10 Illustration of the dynamics of droplet breakup for several xanthan concentrations in the continuous phase and the flow rates  $150 - 12.5mL/min$ : (a)  $C_x = 0\%$ , (b)  $C_x = 0.05\%$ , (c)  $C_x = 0.1\%$ , (d)  $C_x = 0.15\%$ , (e)  $C_x = 0.2\%$ . In each sub-panel the red contours delineate the oil-water interface. . . . . 26
- 11 Temporal evolution of the number  $N$  of connected objects (daughter droplets and filaments) observed in the field of view after the breakup of the single oil droplet for various concentrations of xanthan in the continuous phase indicated in the two inserts and two distinct choices of flow rates: (a) -  $50 - 6.3mL/min$  (b) -  $150 - 12.5mL/min$ . The full lines in each panel are power law fitting functions. . . . . 27
- 12 Probability distributions of the sphericity parameter  $\xi$  of the oil droplets observed in the field of view for various xanthan concentrations in the continuous phase indicated in the top inserts and two combinations of flow rates: (a)  $50 - 6.3mL/min$  (b)  $150 - 12.5mL/min$ . . . . . 28
- 13 **Top row:** Illustration of the front tracking (see Sec. II C for the technical details of the analysis) for a mother droplet in a water matrix and the flow rates  $50 - 6.3mL/min$  at several time instants indicated in the top inserts. The black full line represents the initial contour of the drop, the dashed red its final contour. The black circle is the initial centroid of the drop while the red square is its final centroid. The color map of the velocity vectors relates to their magnitude (red - small values, blue - large values). **Bottom row:** Corresponding probability density functions (pdf's) of the flow type parameter  $\lambda$  computed according to Eq. 7. . . . . 29
- 14 Time series of the shear deformation  $\dot{\gamma}$  (dashed line), extensional deformation  $\dot{\epsilon}$  (full line) and total deformation  $D_2$  (dash-dotted line). The measurements were performed with water as a continuous phase and a combination of flow rates  $50 - 6.3mL/min$ . Micro-graphs of the mother drop acquired at the time instants marked by the full red circles in the main plot are illustrated on the top line. . . . . 30

15	Dependence of the time averaged rates of shear (open symbols) and extension (full symbols) averaged prior to the primary breakup of the mother drop on the xanthan concentration. The symbols refer to the combinations of flow rates indicated in the insert. The lines are cubic spline interpolating functions that serve as a guide for the eye.....	30
16	Statistics of the extensional strains $\epsilon$ prior to the primary breakup at various xanthan concentrations: (a) - time average, (b) - rms of fluctuations. In each panel the symbols refer to the combinations of flow rates indicated in the insert and the lines are cubic spline interpolating functions that serve as a guide for the eye. ....	31
17	Dynamic <b>modes</b> of single oil drop observed in both Newtonian and non-Newtonian fluid matrices. The four experimentally observed dynamic <b>modes</b> detailed in the manuscript are indicated in the legend.....	31

## I. INTRODUCTION

Understanding the physics of deformation of interfaces between [immiscible](#) fluids is of paramount importance for a number of modern day industrial sectors including (but not limited to) pharmaceutical, cosmetics, food, polymer processing, oil field engineering. The emulsification understood as the physical process that transform an equilibrium system of two [immiscible](#) fluids initially separated by a geometrically simple interface into a system consisting of a collection of drops of one fluid suspended into the second is of particular practical interest. The emulsification is typically obtained via a sequence of out of equilibrium processes that lead to the successive deformation and ultimate breakup of initial interface. From a thermodynamic standpoint, the progressive increase in the complexity of the initial interface associated to the emulsification process relates to a drastic increase of the entropy of the system. In isothermal conditions, such entropy increase is solely possible when external mechanical work is supplied to the system, [\[4, 18\]](#). In the case of a two-phase fluid system initially at equilibrium this work is supplied in the form of flow which drives it far away from equilibrium. Environmental considerations including the energy transition which is nowadays an official policy of the European Union call for the use of bio-based fluids as input for the emulsification process (such as biopolymers) [\[17\]](#). Nearly all such environmentally friendly fluids are non-Newtonian which adds a distinct layer of complexity to the emulsification problem as they are characterized by a nonlinear stress-rate of deformation relationship, [\[3\]](#).

Depending on the practical context, the emulsification applications may be sorted into two broad classes. The first class relates to what is generally referred to in the literature as *"drop on demand"* protocols. Thus, when small amounts of emulsions with finely tuned properties (size, dispersity, chemical content) are sought in applications related for example to precise chemical synthesis, encapsulation there exist a number of microfluidic solutions that operate at low throughput (typically smaller than  $mL/h$ ) in a creeping flow regime i.e. at very low Reynolds numbers ( $Re < 0.1$ ), [\[39\]](#).

While the dynamics of the drop formation in low Reynolds microscopic flows of Newtonian fluids is relatively well understood, the case of non-Newtonian still makes the object of current studies. The bulk of studies involving non-Newtonian fluids relates to viscoelastic fluids. Guido and coworkers investigated the deformation of a single drop in a dilute polymer blend for slow steady shear flow by microscopy and image analysis, [\[12\]](#). They conclude that drop orientation in the shear flow is strongly enhanced due to normal stresses of the matrix fluid.

Tretheway and Leal studied experimentally the deformation and relaxation of a Newtonian suspended extensional flow of a Boger fluid, [\[36\]](#). For steady extensional flows, stronger the viscoelasticity of the matrix fluid is, larger the drop deformation becomes.

The viscoelastic behaviour of the continuous phase also influences the breakup dynamics of Newtonian liquid bridges. Derzsi and coworkers studied experimentally the dynamics of a Newtonian liquid stream and the droplet generation in the microfluidic flow focusing device in a viscoelastic continuous phase, [\[7\]](#). They found that the operation regimes in the flow focusing system (dripping without satellites, dripping with single satellites, multiple satellites and jetting) are similar for both Newtonian and non-Newtonian fluids. However, the viscoelasticity tends to stabilize the jets producing relatively smaller droplets by carefully adjusting the viscosity ratio. Nooranidoost and co-workers have studied the effect of the bulk fluid viscoelasticity on droplet formation and dynamics in the flow focusing configuration using numerical method and concluded that the viscoelasticity has a similar effect as decreasing flow rate ratio and thus acts to delay transition from different regimes, [\[26\]](#).

Along with the viscolasticity, [\[14\]](#), the shear-thinning behaviour is important to many industrial applications involving microfluidic droplet fabrication. Ren and coworkers have characterized the breakup dynamics and dripping-to-jetting transitions under various flow conditions in a

Newtonian/shear-thinning multiphase flow focusing micro-system via both experiments and numerical simulations, [29]. For shear-thinning fluids, they show that the droplet size increases when the capillary number is smaller than a critical value, while it decreases when the capillary number is beyond the critical value.

Fragkopoulos and coworkers presented an experimental investigation of the breakup dynamics of toroidal droplets of a Newtonian liquid in a shear thinning continuous phase, [9]. They pointed out that the droplets resist to breakup for times that are longer than those in the linear-behavior Newtonian liquids. By incorporating the non-linearities of the strain rate-dependent viscosity correlation, they scaled the growth rate with the shear strain rate in the breakup point, illustrating that both the viscoelastic and shear-thinning nature of the outside material play a crucial role in the drop dynamics.

The dynamics of slender drop formation using in a microscopic flow focusing device was studied by Fu and coworkers, [10]. Their results indicate that the minimum width of the dispersed thread scales as a power-law with the time for both Newtonian and shear-thinning continuous phases, but with totally different parameters. A similar conclusion was reached by Zhou and coworkers in different type of micro-fluidic device, a T-junction configuration [40]. Chiarello and co-workers have also investigated the effect of the shear-thinning rheology on droplet formation in the  $T$  type microchannel, [5]. They show that the final emulsion drop size may be accurately predicted by knowing the rheology of the bulk continuous phase in advance, [6].

More recently, Agarwal et al. performed a parametric numerical study of the process of droplet formation in a T-junction microchannel with a shear-thinning continuous phase, [1]. Using the Carreau-Yasuda to model the shear-thinning behaviour, they found that higher shear-thinning tends to produce larger droplets with a plug-like shape instead of the spherical one typically observed in the Newtonian case.

The studies concerning with drop dynamics within a shear thinning matrix briefly reviewed above relate to small flow throughput (of the order of  $mL/h$ ) applications or laminar flows. There exist, however, certain practical applications where one to continuously produce emulsions at high throughput using non-Newtonian fluids.

A recent experimental study has investigated the possibility of making such emulsions at flow rates up to  $600mL/min$ , [24]. A systematic study of the dynamics of the emulsification process at high throughput (or Reynolds number) and in the presence of shear thinning rheological behaviour poses a number of formidable theoretical challenges related to the presence of two sources of non-linearity: inertial (related to the large values of the Reynolds number) and rheological (related to the nonlinear stress-strain dependence). A systematic experimental study of the high Reynolds number emulsification in the presence of shear thinning matrix is an equally daunting task as it requires simultaneous measurements of the dynamics of multiple drops and of the flow fields within the continuous phase.

Here we focus on a presumably simpler physical setting consisting of a Newtonian drop that evolves within the turbulent microscopic flow of a shear thinning fluid.

The shear thinning rheological behaviour is often accompanied by viscoelastic effects. In order to study solely the role of shear thinning on the single droplet dynamics we focus through this study on fluids that exhibit a strong shear thinning behaviour but no significant elasticity.

Through the experiments reported herein two coupled sources of nonlinearity are expected to influence the dynamics of a single drop. The first one is of a rheological nature and relates to the shear thinning behaviour of the continuous phase. This should not be confused with the elastic nonlinearity which typically manifests in the presence of strong viscoelastic effects, [3]. The second source of nonlinearity relates to inertial effects which are predominant during turbulent flows.

Several fundamental aspects in relation to both the rheology of the continuous phase and the flow

conditions [are investigated](#): statistics of drop shapes, statistics of drop breakup events, morphology of the dispersed phase fragmented upon the primary breakup of a drop, kinematics of the drop breakup process.

The paper is organized as follows. The experimental methods are described in Sec. II. The choice and rheological properties of the xanthan are briefly described in Sec. II A. The experimental setup, the instrumentation, data acquisition protocol and the data analysis procedure are detailed in Sec. II B. The experimental results are presented in Sec. III which is structured according to the two main physical phenomena the present contribution aims understanding. The dynamics of trapping of individual Newtonian drops within the cross-slot flow are systematically analyzed in Sec. III B. The breakup dynamics of single oil drops are described in Sec. III C. The paper closes with a concise summary of the main findings and a discussion of some perspectives, Sec. IV.

## II. EXPERIMENTAL METHODS

### A. Choice and rheological characterization of the working fluids

#### 1. Choice of working fluids

As a continuous study we have used aqueous solutions of xanthan gum. The xanthan gum is a biopolymer produced by a soil bacterium "*Xanthomonas campestris*" and is one of the most popular hydrocolloids used in various industrial sectors (cosmetics, pharmaceuticals, energy, enhanced oil recovery) applications. This gum is an anionic hetero-polysaccharide consisting of a linear cellulose skeleton of  $\beta$ -D-glucoses of which every second unit is substituted in  $C_3$  by a trisaccharide side chain. Xanthan gum solutions are known to present a significant shear thinning behavior that becomes more pronounced as the polymer concentration is gradually increased [33] but no elasticity. More specifically, several concentration regimes can be encountered according to the polysaccharide concentration used, [31]. The "*dilute regime*" is characterized by small or no steric effects which translates into a weakly shear-thinning behaviour, [37]. Beyond a critical concentration, denoted as  $C^*$ , physical interaction gets significant between molecules, [30]. The corresponding regime is coined as the "*semi dilute regime*". However, internal forces are still dominated by the interactions between the solvent and the polymer [21]. A second critical concentration value,  $C^{**}$ , defines a limit beyond which the system is in the "*concentrated regime*" in the sense that the polymer molecules become entangled. Above the overlap concentration the viscosity increases significantly with the polymer concentration, and a pronounced shear-thinning behavior is observed [37].

The experiments reported herein were performed with a commercial xanthan gum purchased in an anhydrous form (*Keltrol<sup>TM</sup> AP* from Kelco) and dissolved in tap water. The powder was added gradually to the solvent at ambient temperature in a mixing vessel under agitation, using a stirrer. The mixing/dissolution process was carried on for 4 hours in order to achieve complete dissolution and homogenization. The xanthan solutions used through this study were formulated at four different concentrations (0.05%(wt), 0.1%(wt), 0.15%(wt) and 0.2%(wt)). It is difficult to find universal values for bounds of the three concentration regimes  $C^*$  and  $C^{**}$  based on the literature survey described above. This is mainly due to the physico-chemical variety of xanthan gums used by various authors and to the various methodologies applied. However, the range of concentrations tested through this study is mostly consistent with the dilute regime and possibly with the semi-dilute regime for the highest tested concentration used. No preservative or surfactant was used in the formulation.

The addition of polymers is often associated with changes in the interfacial tension. For the

xanthan solutions and the oil used in this study, however, no significant dependence of the interfacial tension  $\sigma_i$  was found. In the range of xanthan concentrations explored the average interfacial tension was found  $\sigma_i = 21.5(\pm 0.3)nN/m$  while the interfacial tension between oil and pure water was  $21.8mN/m$ .

Dilute raw emulsions (5%(v/v)) were obtained by stirring a commercial rape-seed oil into one of the respectively tested continuous phase. The diameters of the oil drops are broadly distributed following a log-normal distribution in between  $D_{min} = 100 \mu m$  and  $D_{max} = 200 \mu m$ .

## 2. Rheological characterisation of the fluids

The rheological behavior of aqueous solutions of xanthan gum is well described by the Carreau-Yasuda model. Within this framework the shear viscosity  $\eta$  is related to the rate of shear  $\dot{\gamma}$  via:

$$\eta = \eta_{\infty} + (\eta_0 - \eta_{\infty}) [1 + (\lambda\dot{\gamma})^2]^{(n-1)/2} \quad (1)$$

Here  $\eta_0 = \lim_{\dot{\gamma} \rightarrow 0} \eta(\dot{\gamma})$  stands for the zero shear viscosity,  $\eta_{\infty} = \lim_{\dot{\gamma} \rightarrow \infty} \eta(\dot{\gamma})$  for the infinite shear viscosity,  $\lambda$  sets a scale ( $1/\lambda$ ) for the shear rate marking the onset of the shear thinning behavior and  $n \in [0, 1]$  is the power law index that characterizes the steepness of the shear thinning behavior observed between the two viscosity plateaus.

As the drop dynamics experiments have been performed at high flow rates in an inertially turbulent regime, it was important to characterize the rheological behavior of the xanthan solutions used in this study in a broad range of shear rates,  $\dot{\gamma} \in [1s^{-1} - 10^5s^{-1}]$ . It is equally important to note that, as the infinite shear viscosity plateau is typically observed at large rates of shear, an accurate fit by the Carreau-Yasuda equally requires varying the shear rates over the broad range above mentioned.

To cover this particularly broad range of shear rates relevant to our study of drop dynamics we have combined conventional rotational rheometry with high shear rate rheometry on a chip, [28].

The high shear rate rheological tests have been performed using a microfluidic rheometer (FLUIDICAM RHEO<sup>TM</sup> from Formulaction, France) which allows one to probe a broad range of shear rates,  $\dot{\gamma} \in [3000s^{-1}, 2 \cdot 10^5s^{-1}]$ . A detailed description of the operating principle of this device can be found in Ref. [32]. The fluid to be characterized is injected side by side with a reference fluid (with a known viscosity) in Y shaped micro-channel with a width  $W_{total} = W + W_R = 2200 \mu m$  as schematically illustrated in Fig. 1. Using successively two microchips with channels of different heights,  $h = 50$  and  $150 \mu m$  allows to cover the above cited shear rates range.

The flow rates  $Q_R$ ,  $Q$  of the reference fluid and of the fluid to be characterized are precisely controlled using two accurate micro-syringe pumps. As a reference Newtonian fluid, a solution of polyethylene glycol (PEG) with a viscosity of  $\eta_R = 6.85 mPa \cdot s$  at  $T = 25^\circ C$ .

Due to the small size of the channel the flows are laminar and fully developed at the channel outlet. Thus, the ratio of the transverse extents of the two fluids  $W/W_R$  near the outlet of the micro-fluidic device is proportional to the ratio of the apparent viscosity  $\eta_{app}$  of the fluid to be characterized and the known viscosity  $\eta_R$  of the reference fluid, [13, 25] :

$$\frac{W}{W_R} = \frac{\eta_{app}}{\eta_R} \frac{Q}{Q_R} \quad (2)$$

Thus, according to the simple relationship above, monitoring optically the ratio  $\frac{W}{W_R}$  and knowing the flow rates  $Q, Q_R$  allows one to extract the ratio  $\frac{\eta_{app}}{\eta_R}$  between the apparent viscosity of the

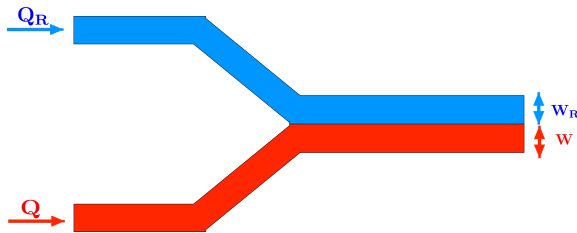


FIG. 1: Schematic representation of the high shear rate microfluidic rheometer:  $Q$  - flow rate of the fluid to be characterized,  $Q_R$  - flow rate of the reference fluid with a known viscosity,  $W$  - **transverse** extent of the fluid to be characterized,  $W_R$  - **transverse** extent of the reference fluid.

fluid to be characterized to the known viscosity of the reference fluid. The ratio  $\frac{W}{W_R}$  is accurately measured by acquiring a time series of images of the interface between the two fluids and subsequent image processing.

The true rate of shear experienced by the fluid to be characterized may be expressed according to Weissenberg-Rabinowitsch-Mooney equation, [20]:

$$\dot{\gamma}_{true} = \frac{\dot{\gamma}_{app}}{3} \left[ 2 + \frac{d \ln \dot{\gamma}_{app}}{d \ln \tau} \right] \quad (3)$$

where  $\dot{\gamma}_{app} = \frac{6Q}{Wh}$ ,  $h$  is the height of the micro-channel, [22] and  $\tau = \dot{\gamma}_{true}\eta = \dot{\gamma}_{app}\eta_{app}$  is the true stress imposed onto the tested fluid. High shear rate viscosities are shown in Fig. 2(a) as empty symbols.

The classical rotational rheometry tests were performed using a Mars III (ThermoFischer Scientific) device which is a controlled stress rotational rheometer equipped with a nano-torque module. Tests were performed using a cone and plate geometry with a radius  $R = 30 \text{ mm}$  and a truncation angle  $\alpha = 2 \text{ deg}$  ( $C60/2 \text{ TiL}$  for HAAKE MARS). The temperature was regulated at  $25 \pm 0.05^\circ\text{C}$  using both a Peltier system embedded in the bottom plate of the rheometer and an electrical oven enclosure mounted on the top of the geometry. The number of steps for each branch of the ramp was  $N = 100$  and the averaging time per step was  $30 \text{ s}$ . Measurements have been performed by imposing increasing/decreasing controlled shear rate ramps ranging from  $1 \text{ s}^{-1}$  to a maximal shear rate  $\dot{\gamma}_c$  beyond which inertial instabilities are expected to occur within the cone-plate flow. Such rotational measurements are shown as full symbols in Fig. 2(a).

The critical shear rate  $\dot{\gamma}_c$  corresponds to a critical value of Reynolds number  $Re_c$  above which the cone-plate flow turns inertially unstable (and thus it is no longer a rheometric flow). As we are not aware of any analytical result predicting the value of  $Re_c$  for a cone-plate geometry for a shear thinning fluid, we have (rather arbitrarily) chosen  $Re_c = 0.1$ . However, the determination of the critical shear rates  $\dot{\gamma}_c$  corresponding to the onset of the inertial (non-rheometric) flow regime is not straightforward which calls for a detailed description. First, high shear rate viscosity data has been obtained according to the procedure detailed above. Next, we have retained only the rotational rheological data corresponding to  $\dot{\gamma} < 100 \text{ s}^{-1}$  and performed a first rough non linear fit of these data combined with the high shear rheometry data according to the Carreau- Yasuda model, Eq. 1. This rough nonlinear fit allows one to compute the Reynolds numbers corresponding



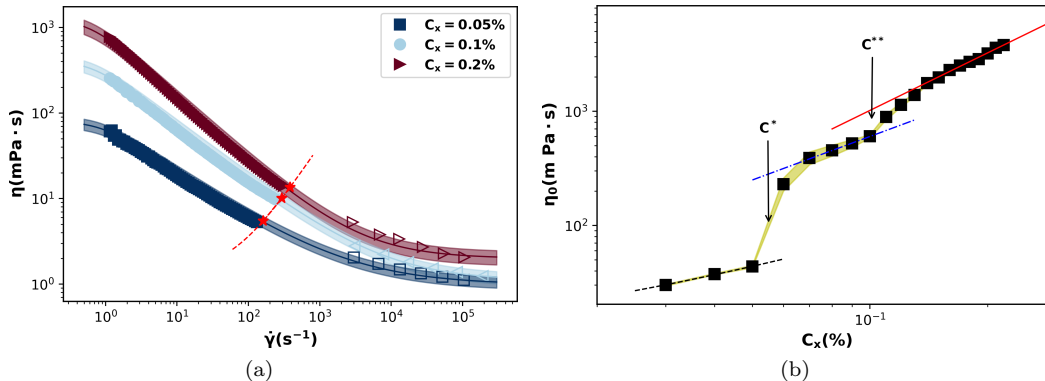


FIG. 2: (a) Rheological flow curves measured for three distinct xanthan concentrations indicated in the insert via two alternative techniques (see text for description): classical rotational rheology - full symbols, microfluidic high shear rate rheology - open symbols. The full lines are nonlinear fitting functions obtained according to the Carreau-Yasuda model and the highlighted regions indicate the confidence interval of the fitting procedure. The stars and the dashed line mark the critical line  $(\dot{\gamma}_c, \eta_c)$  defined by the condition  $Re_c = 0.1$  that defines the inertia-free range of the classical rotational rheology measurements (see text for details/discussion). (b) Dependence of the zero shear viscosity  $\eta_0$  on the concentration of xanthan  $C_x$ . The lines are power law fitting functions (see text for description). The vertical arrows point the concentration bounds  $C^*$ ,  $C^{**}$  of the relevant concentrated regimes.

to the rotational measurements according to:

$$Re = \frac{\rho (R \tan \alpha)^2 \dot{\gamma}}{\eta_\infty + (\eta_0 - \eta_\infty) [1 + (\lambda \dot{\gamma})^2]^{(n-1)/2}} \quad (4)$$

where  $\rho$  is the density of the xanthan solution. Next, the maximal values of shear rates  $\dot{\gamma}_c$  have been computed using Eq.4 and the condition  $Re(\dot{\gamma}_c) = 0.1$ .

We illustrate combined measurements of the shear viscosity performed for three distinct concentrations of xanthan in Fig. 2(a).

A nonlinear fit based on the Levenberg-Marquardt algorithm according to the Carreau-Yasuda model has been performed on the rotational data corresponding to  $\dot{\gamma} < \dot{\gamma}_c$  and to the high shear rate data - see the full lines in Fig. 2(a). The confidence bounds of the nonlinear fitting functions shown as highlighted regions account for roughly 15% – 20% of the measured value of the viscosity. The bounds of the inertial regime are marked with stars in Fig. 2(a).

To identify various concentration regimes relevant to the drop dynamics experiments reported herein, we illustrate in Fig. 2(b) measurements of the zero shear viscosity performed in a range of xanthan concentrations  $C_x$  relevant to our experiments. For low concentrations of xanthan,  $C_x \leq 0.05\%$  the zero shear viscosity increases linearly with the xanthan concentration (the dashed line in Fig. 2(b)) which is what one would expect for a dilute concentration regime. Past a critical value of the xanthan concentration  $C^* \approx 0.05\%$  a power law scaling of the zero shear viscosity with the xanthan concentration is observed,  $\eta_0 \propto C_x^{1.26 \pm 0.12}$  is observed. We identify this range of concentrations with the so called semi-dilute regime. Increasing the xanthan concentration even

further past  $C^{**} \approx 0.1\%$  a third scaling regime is observed  $\eta_0 \propto C_x^{1.67 \pm 0.15}$ . This corresponds to the so called "concentrated" concentration regime.

To our best knowledge, data on the scaling of the zero shear viscosity with the xanthan concentration are rather scarce in the literature. We compare in the following our scaling results with those obtained by Nsengiyumvaa and Alexandridisa. [27]. As a polymer, they have used Keltrol T 622, Mat. #20000625 by CP Kelco (while we used a slightly different grade, Keltrol AP). The scaling behavior they found within the semi-dilute regime is very different than ours ( $\eta_0 \propto c^{0.5}$  while we found  $\eta_0 \propto c^{1.2}$ ). On the other hand, the scaling behaviour they found in the concentrated regime is closer to ours ( $\eta_0 \propto c^{1.5}$  while we found  $\eta_0 \propto c^{1.67}$ ). We attribute these discrepancies to several factors: differences in the grade of xanthan, differences in the salt content of the solutions (our solutions were prepared in tap water so their ionic content was not controlled) and possible differences in the rheometric procedure.

The bulk of the droplet dynamics experiments reported herein correspond the semi-dilute and concentrated concentration regimes.

## B. Experimental setup

### 1. Microscopic flow channel

The experiments have been conducted in a cross-slot micro-channel schematically illustrated in Fig. 3. The micro-channel was machined from an acrylic block with the dimensions  $70 \text{ mm} \times 40 \text{ mm} \times 18 \text{ mm}$  using a fast spinning ( $14000 \text{ rot/min}$ ) micro-milling head (Nakanishi, model HES510 – BT40) mounted on a commercial computer controlled milling machine (Twinhorn, model VH1010). This micro-milling technique has been previously used in microfluidics, [19, 23].

By a precise alignment of the initial acrylic block on the stage of the milling machine, the depths of the micro-channel was accurately controlled over its entire length with an end to end variation smaller than one percent. The average roughness of the edges of the micro-channel as resulted from the micro milling process is roughly of the order of a micron which accounts for less than a percent of the channel width. The edge smoothness obtained with this micro-machining technique is comparable to that obtained via the classical micro lithography techniques used to produce PDMS micro-channels, [35]. However, unlike the more popular PDMS micro-channels, the micro-milled micro-channels are able to sustain very large pressure up to  $90 \text{ bars}$  which is essential for performing experiments at very high volumetric flow rates. The channel is closed by a second acrylic block fitted with o-rings to prevent fluid leakage via a set of stainless steel bolts, Fig. 3(a).

The geometry of the micro-channel is detailed in Fig. 3(b). This cross-slot geometry has been proposed and studied by A. Belkadi and his coworkers for the case of Newtonian fluids, [2]. The solution carrying the single oil drop, i. e. dilute raw emulsion, is fed through an inlet with a rectangular cross-section  $H_1 = W_1 = 300 \mu\text{m}$  at a mass flow rate  $\dot{m}_{i1}$  while a droplet free stream of xanthan solution is fed through an opposite inlet with dimensions twice larger  $H_2 = W_2 = 600 \mu\text{m}$  at a mass flow rate  $\dot{m}_{i2}$ , top panel of Fig. 3(b). The un-even dimensions of the two fluid inlets have been purposely chosen in order to generate a swirling flow motion at the impact between the two fluid streams depicted in the cartoon illustrated in the bottom panel of Fig. 3(b). This swirling motion promotes the transition to turbulent flow states which plays a crucial role in the breakup dynamics of the single oil drop.

After impacting within the impingement region highlighted by the red squares shown in Fig. 3(b) the fluids are discharged through two identical outlets. The two channel outlets have a rectangular cross section,  $H = W = 600 \mu\text{m}$ . The flow rates of the discharged fluids are found to be equal

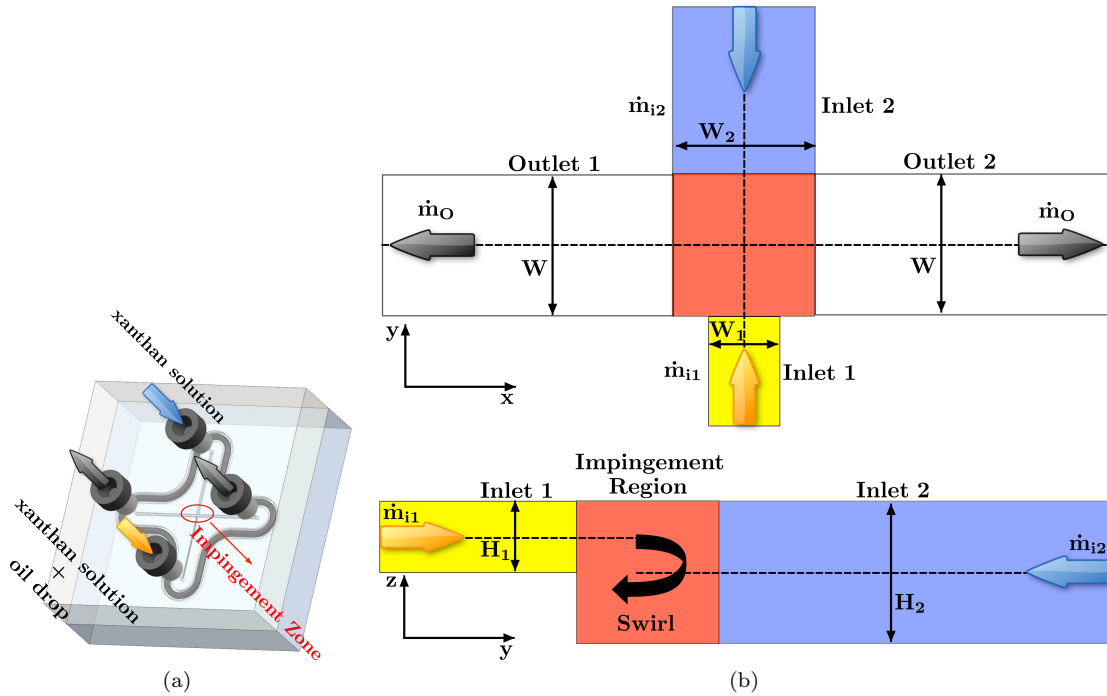


FIG. 3: (a) Schematic view of the microfluidic chip. (b) **Top:** Frontal (camera) view of the cross-slot region in the  $(x, y)$  plane. **Bottom:** Lateral view (not accessible through our measurements but only hinted as) of the cross-slot region in the  $(y, z)$  plane. The colors are as follows: blue and yellow regions refer to the channel inlets while the red highlighted region is the impingement zone. The "cartoon" arrow is solely a visual hint for the three dimensional flow structure dominated by the presence of a swirl located at the centre of the cross-slot region later referred to in the paper.

(within 1%). The mean velocity at the outlets  $U_O$  is obtained by measuring the outlet flow rates  $\dot{m}_{o1} = \dot{m}_{o2} = \dot{m}_o$ , [2, 16].

Various experiments are referred to by specifying the pair of the volumetric flow rates of the inlet fluids  $Q_{i_2} - Q_{i_1}$ .

## 2. Data acquisition system

The flow control and data acquisition system are schematically illustrated in Fig. 4. The two fluids injected through the inlets of the micro-channel are held in the fluid containers  $\mathbf{IFC}_{1,2}$ . The two inlet fluid containers are mounted on two identical digital balances  $\mathbf{DB}_{1,2}$  (Sartorius-MSE 2203) which, connected to a personal computer  $\mathbf{PC}_1$ , provide a real time measurements of the flow rates  $\dot{m}_{i1,2}$ . The inlet fluids are pumped into the micro-channel chip  $\mathbf{MFC}$  by two pumps  $\mathbf{P}_{1,2}$  (*AP TRIX* 500 from Armen, France). The fluids collected through the two outlets of the micro-channel are discharged in an outlet fluid container  $\mathbf{OFC}$ . The micro-channel is illuminated

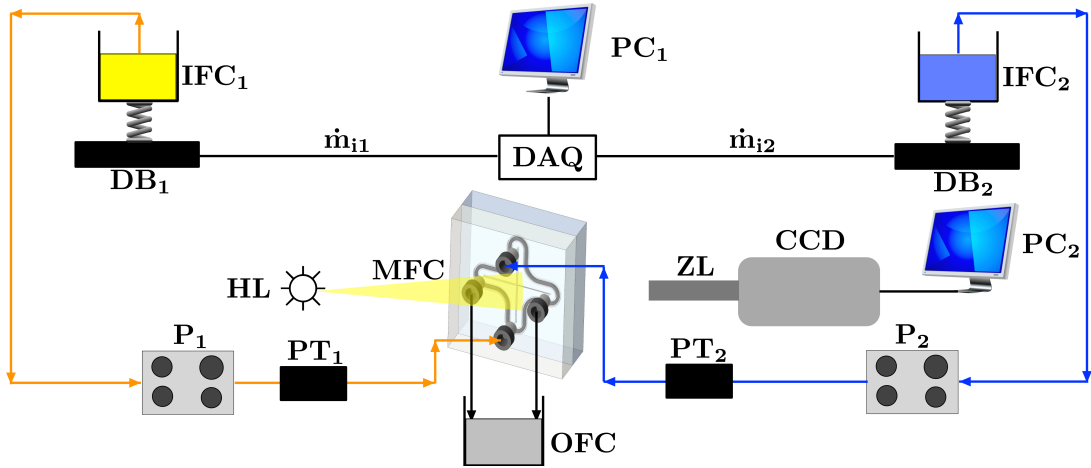


FIG. 4: Schematic representation of the experimental system for the visualization of single drop dynamics:  $\text{IFC}_{1,2}$  - input fluid containers,  $\text{OFC}$  - output fluid container,  $\text{DB}_{1,2}$  - digital balances,  $\text{P}_{1,2}$  - fluid pumps,  $\text{PT}_{1,2}$  - pressure transducers,  $\text{PC}_{1,2}$  - data acquisition computers,  $\text{MFC}$  - microfluidic chip,  $\text{HL}$  - halogen lamp,  $\text{CCD}$  - digital camera,  $\text{ZL}$  - zoom lens.

from behind by a 50 W halogen lamp  $\text{HL}$  with its optical axis normally aligned to the centre of the impingement region of the micro-channel. The impingement region is visualised by a fast camera  $\text{CCD}$  (*FASTCAME SA – X2 1080K M<sub>4</sub>* from Photron) equipped with a 12 $\times$  magnification zoom lens  $\text{ZL}$  (Lavision) and connected to a second personal computer  $\text{PC}_2$ . The fast camera is equipped with an image intensifier and can be operated up to the nominal frame rate of 1080 *kfps*. For the bulk of the experiments reported herein the camera has been operated at 300 *kfps* and, occasionally, at 150 *kfps*. To maximize the signal to noise ratio of the images, a maximum exposure time of 1/583784 s has been set.

### C. Data analysis

The main data analysis tool relates to the processing of individual flow images which allows one to extract the contour of each object (mother or daughter droplets) from each image.

For this purpose, a dedicated image processing package has been developed in-house using the scikit-image module of Python, [38]. Several image analysis steps are illustrated in Fig. 5.

The main steps of the image processing sequence are illustrated in Fig. 5(a). The first step consists of computing an average background of 3000 individual flow images similar to the one illustrated in panel (a). Next, the background is subtracted from each image of the sequence and the contrast of the resulting image is enhanced using an adaptive histogram equalization technique, panel (b). Note that after the subtraction of the background some features visible in panel (a) and related to impurities present on the channel walls are no longer visible and solely the details of the drops are retained. A binary closure of the enhanced image is performed and individual objects (mother droplet and/or daughter droplets) are detected in each flow image, panel (c). Finally, the

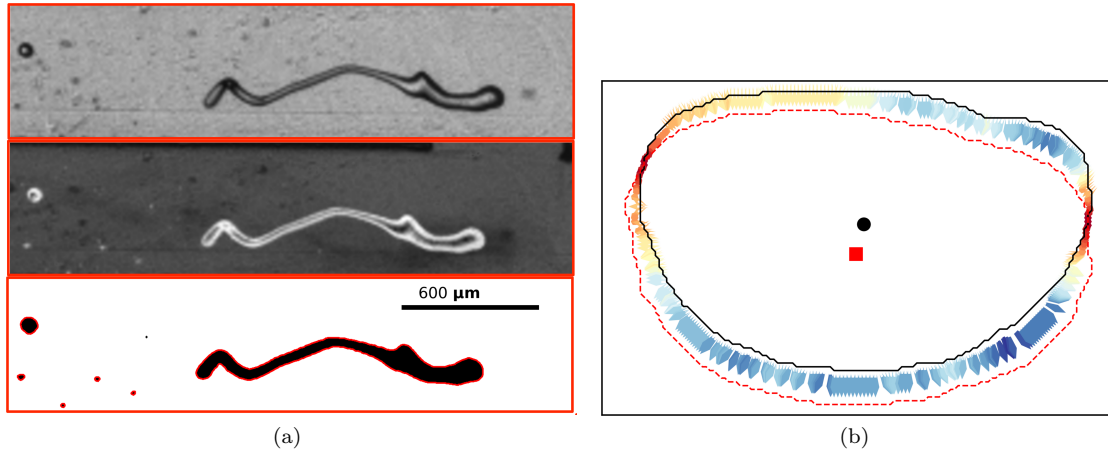


FIG. 5: (a) Illustrations of the image processing sequence: **Top:** Original image **Middle:** Image after subtracting the background and enhancing the contrast **Bottom:** Binary closed image with the contours of the identified objects (droplets) superposed. (b) Illustration of the front tracking for a mother droplet in a water matrix and the flow rates  $50 - 6.3 \text{ mL/min}$ . The black full line represents the initial contour of the drop, the dashed red its final contour. The black circle is the initial centroid of the drop while the red square is its final centroid. The color map of the velocity vectors relates to their magnitude (red - small values, blue - large values).

contours and centroids of each object detected in each of the images of the sequence are saved in a text file together with the corresponding time stamp.

This output text file will later serve for assessing several physical quantities relevant to the dynamics of a single drop in the turbulent cross-slot flow which will be detailed later through the manuscript.

We chose to detail here only one particular processing step we have implemented in order to quantitatively assess the flow kinematics during the dynamics of the droplet. To assess the kinematics of the droplet deformation process, one needs to obtain information of the flow field around it. Such information is typically obtained by means of microscopic Particle Image Velocimetry (micro-PIV). Micro-PIV measurements require seeding the matrix fluid with sub-micron tracers and insuring an illumination of the flow that is generally inconsistent with the white light visualization of drops. Additionally, the light scattered by the flow tracers is proportional to their cubic radius and the frame rate of the image acquisition process is very large (adapted to the large volumetric flow rates of interest). Thus, one needs extremely powerful light sources that are technically problematic to use without overheating the flow channel during the data acquisition process.

Here we propose an alternative and simple technique that renders the distribution of the velocity along the drop contour in the  $(x, y)$  plane which in turn may provide useful information on the flow kinematics. The technique relies on the detection of the drop contour from each frame and is implemented following the steps described below.

The key step of such measurements is to obtain the distribution of the velocity along the contour of the deforming mother drop by a particle tracking algorithm developed in-house that tracks the displacement of each point of the drop contour between successive frames. We illustrate this front tracking procedure in Fig. 5(b).

Considering the velocity gradient tensor  $\nabla\mathbf{U}$  where  $\mathbf{U} = (u_x, u_y)$  is the two dimensional vector field measured along the contour of the deforming mother droplet, the strain rate tensor is defined as  $\mathbf{D} = \nabla\mathbf{U} + \nabla^T\mathbf{U}$ . The global deformation rate of the mother drop is quantified by the second invariant of the strain-rate tensor:

$$D_2 = (2\mathbf{D} : \mathbf{D})^{1/2} = \left\{ 2 \left[ \left( \frac{\partial u_x}{\partial x} \right)^2 + \frac{1}{2} \left( \frac{\partial u_x}{\partial y} + \frac{\partial u_y}{\partial x} \right)^2 + \left( \frac{\partial u_y}{\partial y} \right)^2 \right] \right\}^{1/2}. \quad (5)$$

The turbulent flow field in the impingement flow region is a rather complex mixture of shear, pure strain (extension) and rigid body rotation.

While the rigid body rotation mainly takes place in the third dimension and can not be inferred by the two-dimensional imaging of the mother drop reported herein, the relative contributions of the shear and extension to the overall deformation of the mother drop may be quantitatively assessed by the defining the non-dimensional flow parameter defined implicitly via [11]:

$$\nabla v = D_2 \begin{bmatrix} 0 & 1 & 0 \\ \lambda & 0 & 0 \\ 0 & 0 & 0 \end{bmatrix} \quad (6)$$

Explicitly, the flow type parameter  $\lambda$  may be written in terms of the second invariant of the rate of deformation tensor  $D_2$  and the vorticity  $\omega$ :

$$\lambda = \frac{D_2 - \omega}{D_2 + \omega} \quad (7)$$

where  $\omega = \frac{\partial u_y}{\partial x} - \frac{\partial u_x}{\partial y}$  is the magnitude of the vorticity.

A pure straining flow corresponds to  $\lambda \rightarrow 1$  while a pure shear flow corresponds to  $\lambda \rightarrow 0$ . Finally, the effective strength of the straining flow may be crudely estimated as  $\dot{\epsilon} \approx \lambda D_2$  and that of the shear flow as  $\dot{\gamma} \approx (1 - \lambda) D_2$ .

### III. RESULTS

#### A. Summary of the experiments

The experiments have been performed using as a continuous phase five distinct xanthan solutions with concentrations  $C_x$  ranging from 0%(wt) (pure water) to 0.2%(wt). For each value of the xanthan concentration five distinct pairs of flow rates at the two channel inlets have tested.

The dynamic behaviour of single oil drops in the flow of the xanthan solutions is governed by an interplay between inertia, viscous effects and capillarity, [8]. It is therefore interesting to estimate the strength of each contribution for the background flows we study.

The drop Reynolds numbers are estimated according to  $Re_d = \frac{\rho U_o D}{2\eta_x}$  where  $U_o$  is the mean outlet velocity and  $D$  is the initial diameter of the mother drop which ranges between [100  $\mu\text{m}$ , 200  $\mu\text{m}$ ]. The bulk Reynolds number is defined by  $Re = \frac{\rho U_{i2} H_2}{\eta_x}$ . The viscosities of the xanthan solutions are obtained by interpolation of the rheological flow curves corresponding to the mean shear rates estimated using the flow rates,  $\dot{\gamma} = \frac{2Q_{i2}}{H_2 W_2^2}$ . As one can see from the values of the bulk Reynolds number listed in table I, the flows we study are either weakly or fully developed turbulent.

TABLE I: Summary of the experiments.  $C_x$  stands for the xanthan concentration,  $Q_{i1}, Q_{i2}$  for the volumetric flow rates,  $Re_d$  for the drop Reynolds number and  $Re$  for the bulk Reynolds number.

$C_x(\%wt)$	$Q_{i2}(mL/min)$	$Q_{i1}(mL/min)$	$Re_d$	$Re$
[0, 0.2]	50	6.3	[38.8, 276]	[305, 1530]
	50	9.4	[34.7, 280]	[305, 1530]
	50	12.5	[37.1, 240]	[305, 1530]
	100	12.5	[69.3, 463]	[659, 3053]
	150	12.5	[190, 749]	[1021, 4582]

As already stated through the paper, such flows have been previously employed for producing emulsions at high throughput, [15, 16].

Liquid–liquid dispersion and the background flow in the microfluidic device were experimentally investigated in a broad range of flow rates, [15, 16]. Through these experiments the Reynolds number (estimated for the continuous aqueous phase, not by using the droplet size) was varied from 1000 to 7000 and the oil dispersed volume fraction varied between 3% and 30%. The rather large values of the Reynolds number indicate that the background flow was either weakly or fully developed turbulent. This observation has been reinforced by measurements of the pressure drops and the qualitative observation of spatially irregular clouds of dispersed droplets, [15]. A more systematic space-time analysis of the background flow by means of time-resolved micro-PIV is underway and will be reported shortly in a subsequent paper.

The balance between the viscous effects and the combined inertia and capillarity is quantified by the Ohnesorge number:

$$Oh = \frac{\eta}{(\rho\sigma_i D_{av})^{1/2}} \quad (8)$$

where  $\rho$  is the density of the solutions,  $\sigma_i = 21.5mN/m$  the interfacial tension,  $\eta$  is a scale for the viscosity and  $D_{av} = 150\mu m$  is the average diameter of the injected drops. As the flows we consider are driven in range of high shear rates ( $\dot{\gamma} > 10^3 s^{-1}$ ), one may consider as a scale for the viscosity  $\eta$  the infinite shear viscosity  $\eta_\infty$  which, according to the data presented in Fig. 2(a), varies between 1.3 *mPas* and 3 *mPas*. With these remarks, one may conclude that through our experiments the Ohnesorge number was varied between  $Oh \in [2.28 \cdot 10^{-2}, 5.2 \cdot 10^{-2}]$ . The small values of the Ohnesorge number indicate that the flows are dominated by the inertia and the capillarity rather than by viscous effects.

In the presence of inertia, viscous effects and capillary forces there exist three intrinsic time scales relevant to the dynamics of the single drop. The inertio-capillary time  $\tau_{ic} = \left(\frac{\rho D_{av}^3}{\sigma_i}\right)^{1/2}$  can be estimated  $\tau_{ic} \approx 0.4ms$ . The visco-inertial time  $\tau_{vi} = \frac{\rho D_{av}^2}{\eta^2}$  varied in between  $\tau_{vi} \in [2.5 s, 13 s]$ . Last, the Ohnesorge characteristic time  $t_O = \frac{\eta^3}{\rho\sigma_i^2}$  was varied in the interval  $\tau_O \in [4.74 ns, 58.3 ns]$ .

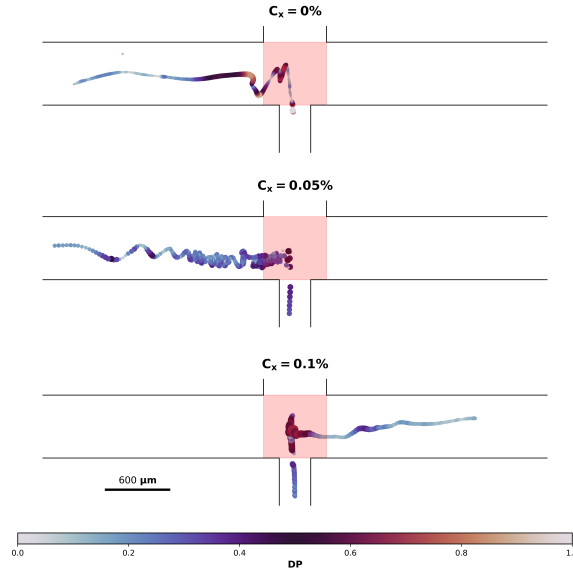


FIG. 6: Illustrations of single droplet dynamics for several xanthan concentrations indicated in the top inserts and flow rates are  $50 - 6.3 \text{ mL/min}$ . The scatter refers to the instantaneous positions of the centre of mass of the oil droplet. Both the false color and the relative size of the symbols map the deformation parameter  $DP$ . In each panel the red highlighted zone marks the impingement region.

### B. Trapping and deformation dynamics of a single oil droplet for various xanthan concentrations in the continuous phase.

A first aspect we focus on relates to the dynamics of trapping and deformation of single oil droplets within the impingement flow region in cases when no breakup occurs for various concentrations  $C_x$  of xanthan in the continuous phase. The effective deformation of the drop may be quantitatively described by the non-dimensional deformation parameter  $DP$  initially introduced by G. I. Taylor, [34]:

$$DP = \frac{L - B}{L + B} \quad (9)$$

where  $L$ ,  $B$  are the major and minor semi-axis of the drop, respectively.

The dynamics of a single oil droplet for various concentrations  $C_x$  of xanthan in the continuous phase are illustrated in Fig. 6 where successive positions of a single drop color coded by the value of the deformation parameter  $DP$  are plotted. As the concentration of xanthan in the continuous phase is gradually increased, the droplet spends more time within the impingement region highlighted by a red square.

A clear variation of the instantaneous droplet deformation along its trajectory is noticeable in Fig. 6. For the case of pure water ( $C_x = 0\%$ ) as a continuous phase, the droplet does not deform significantly while being trapped within the impingement region but deforms considerably after



escaping this region following some sort of "sling shot" effect. For the shear thinning cases we have explored ( $C_x = 0.05\%$ ,  $C_x = 0.1\%$ ) the droplet first deforms within the impingement region then relaxes for a short period of time while exiting the impingement region then gets deformed once more following a similar type of "sling shot" effect. More insights into the temporal dynamics of the droplet trapping process may be obtained by focusing on time series of the deformation parameter, their corresponding probability distributions and the average trapping times, Fig. 7.

For the case of pure water as a continuous phase large fluctuations of the deformation parameter are observed by mostly of low frequency, Fig. 7(a). For a xanthan concentration  $C_x = 0.05\%$  in the continuous phase the magnitude of fluctuations of the deformation parameter remain large but now high frequency details are visible in the time series. For the highest xanthan concentration illustrated, the level of the high frequency fluctuations decreases. Thus, qualitatively speaking, the time series of the deformation parameter do not seem to follow a monotonic trend with increasing concentration of xanthan in the continuous phase. This lack of a monotonic trend is, perhaps, even more visible while plotting the probability density functions of the deformation parameter  $DP$ , Fig. 7(b). For the case of pure water, the pdf is double peaked. For a xanthan concentration  $C_x = 0.05\%$  the pdf becomes singly peaked but a further increase of the xanthan concentration  $C_x = 0.1\%$  brings us back to an even more pronounced (than in the pure water case) doubly peaked shape. Yet, the trapping time  $t_{trapping}$  (defined as the time spent by the drop within the impingement region marked by a red rectangle in Fig. 6) and the time averaged droplet deformation  $\langle DP \rangle_t$  increase monotonically (basically linearly) with increasing concentration of xanthan in the continuous phase, Fig. 7(c).

In an attempt to correlate the trapping dynamics of the individual droplet and deformation with their velocity, we present in Fig. 7(d) probability density functions (pdf's) of the in plane velocity measured for the cases illustrated in Fig. 6.

As the xanthan concentration is gradually increased no clear trend in the shape of the pdf's may be observed. This is most probably coming from the fact that the flow within the impingement region is genuinely three dimensional while, experimentally, we solely have access to a two dimensional flow field.

It is equally instructive to monitor the probability of the droplet trapping for various xanthan concentrations in the continuous phase as a function of the flow conditions (combination of flow rates), Fig. 8(a). For the first three driving flow rates ( $50 - 6.3mL/min$ ,  $50 - 9.4mL/min$ ,  $50 - 12.5mL/min$ ) the trapping probability decreases when the xanthan concentration  $C_x$  gradually increases - the circles, squares and triangles in Fig. 8(a). For the highest flow rates investigated ( $100 - 12.5mL/min$ ,  $150 - 12.5mL/min$ ) the trend of the probability with the xanthan concentration is reversed, the diamonds and stars in Fig. 8(a).

This *inversion* of the trend of the trapping probability with the xanthan concentration observed while switching from low to high driving flow rates indicates a significant change in the dynamics of the single droplet as the concentration of xanthan is gradually increased.

In order to rationalize the various single droplet dynamics observed within the impingement region in terms of the flow structure we first note that the impingement region is dominated by the presence of a three dimensional swirling motion sketched in the bottom panel of Fig. 3(b). This swirling motion originates from the uneven sizes of the two fluid inlets, top panel of Fig. 3(b) and promotes the transition to turbulent flow states, [2].

In the absence of three dimensional measurements of the flow fields within the impingement region, the effective strength of this swirling motion may be estimated as:

$$\Psi_{eff} = SSI \left( \frac{\eta_w}{\eta_x} \right) \quad (10)$$

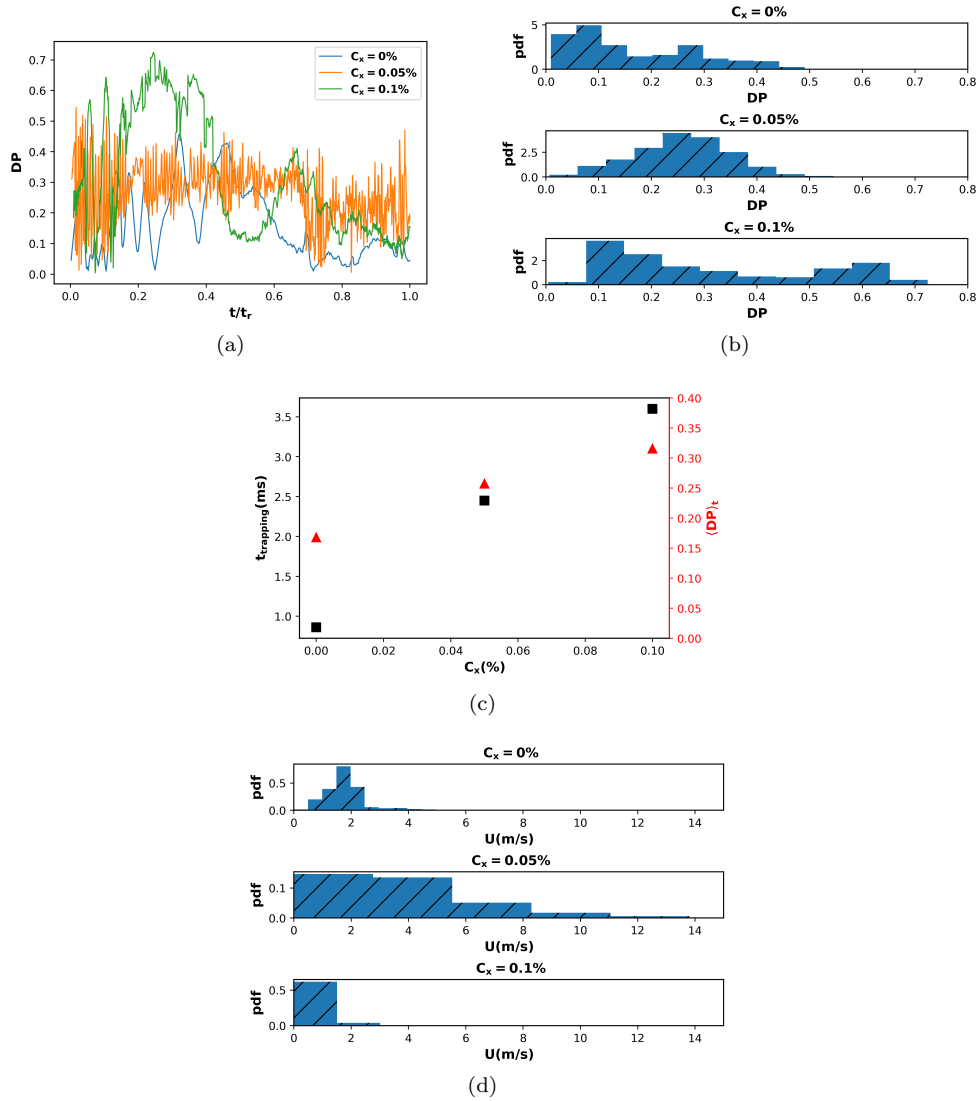


FIG. 7: (a) Time series of the deformation parameter  $DP$  corresponding to the data illustrated in Fig. 6. The time axis is normalized by the residence time  $t_r$  of the drop in the field of view. (b) Probability density functions corresponding to the time series illustrated in panel 7(a). (c) Summary of the trapping statistics: bottom-left axis - dependence of the trapping time  $t_{trapping}$  on the concentration of xanthan in the continuous phase, bottom-right - dependence of the time averaged deformation parameter  $\langle DP \rangle_t$  on the xanthan concentration. (d) Probability density functions of the in plane velocity of an oil droplet exhibiting trapping behaviour for three concentrations  $C_x$  of xanthan in the continuous phase indicated in the top inserts.

where the non-dimensional swirl strength index  $SSI$  previously introduced in Ref. [16] is defined using the flow rates of the fluids fed through the inlets 1, 2 of the micro-channel:

$$SSI = \frac{m_{i1} \bar{U}_{i1}^2 \frac{\bar{U}_{i1}}{\bar{U}_{i1} + \bar{U}_{i2}} d + m_{i2} \bar{U}_{i2}^2 \frac{\bar{U}_{i2}}{\bar{U}_{i1} + \bar{U}_{i2}} d}{m_0 \bar{U}_0^2 H} \quad (11)$$

Here  $m_{i1} = \rho Q_{i1}$ ,  $m_{i2} = \rho Q_{i2}$  stand for the mass flow rates of the fluids injected through the inlets 1, 2 of the micro-channel,  $m_0 = \rho Q_o$  is the flow rate measured through each of the outlets of the micro-channel and  $\bar{U}_{i1}$ ,  $\bar{U}_{i2}$ ,  $\bar{U}_o$  are the corresponding flow speeds. Here  $H = H_2$  is the size of the outlets and  $d = \frac{H_2 - H_1}{2}$  is the offset distance between the symmetry axis of the inlets.

The definition of the effective swirl strength in the presence of shear thinning is chosen on a rather intuitive basis so its value decreases as the viscosity  $\eta_x$  of the continuous phase increases (upon of a gradual increase of the xanthan concentration).

The viscosity of the xanthan solution involved in the definition of the effective swirl strength by Eq. 10 is computed via interpolation of the rheological measurements described in Sec. II A 2 and illustrated in Fig. 2(a) at values of the effective shear rate estimated using the flow rates.

The dependence of the probability for a single oil droplet of being trapped in the impingement region computed by monitoring 100 individual trapping events (droplets) on the flow parameter  $\Psi_{eff}$  is shown in Fig. 8(b).

For low values of the effective flow parameter,  $\Psi_{eff} \leq 0.1$ , no droplet trapping events are observed.

When plotted against the effective swirl efficiency parameter  $\Psi_{eff}$ , the trapping probabilities measured when xanthan solutions are used as a continuous phase follow a common trend,  $P_t \propto (\Psi_{eff} - \Psi_{eff}^c)^{0.5}$  with  $\Psi_{eff}^c \approx 0.1$  while the data acquired with water as a continuous phase fall clearly off this trend, Fig. 8(b). The square root trend observed for the xanthan data indicates that, as the effective swirl strength is gradually increased past the critical value  $\Psi_{eff}^c \approx 0.1$ , trapping events emerge via an imperfect bifurcation.

### C. Breakup dynamics of a single oil droplet for various xanthan concentrations in the continuous phase

A second interesting physical aspect relates to the dynamics of the breakup process of a single oil drop as a function of the shear thinning rheology of the continuous phase. Understanding the breakup dynamics of a single drop is a key step towards understanding the emulsification process which is relevant to a number of applications in various engineering settings.

The physical quantity that is the most straightforward to assess is the time needed for a mother drop to undergo a primary breakup event. To assess this, we perform statistics over 100 individual mother drops tracked from the moment they entered the impingement region till until the primary breakup event occurred.

The dependence of the average breakup time  $t_b$  measured for various flow rates indicated in the top insert on the xanthan concentration  $C_x$  is shown in Fig. 8(c). The full lines are cubic spline interpolating functions that serve as a guide to visualise the trend of the data. The breakup times are closest in magnitude to the inertio-capillary time scale  $\tau_{ic} \approx 0.4 \text{ ms}$  but separated by roughly three orders of magnitude from both the Ohnesorge time scale  $\tau_O$  and the visco-inertial time scale  $\tau_{vi}$ . This indicates that inertio-capillary effects control the single drop breakup process. Corresponding to the low flow rates explored the dependence of the breakup time on the xanthan concentration is non monotonic and exhibits a peak around  $C_x \approx 0.05$  (the circles, squares and

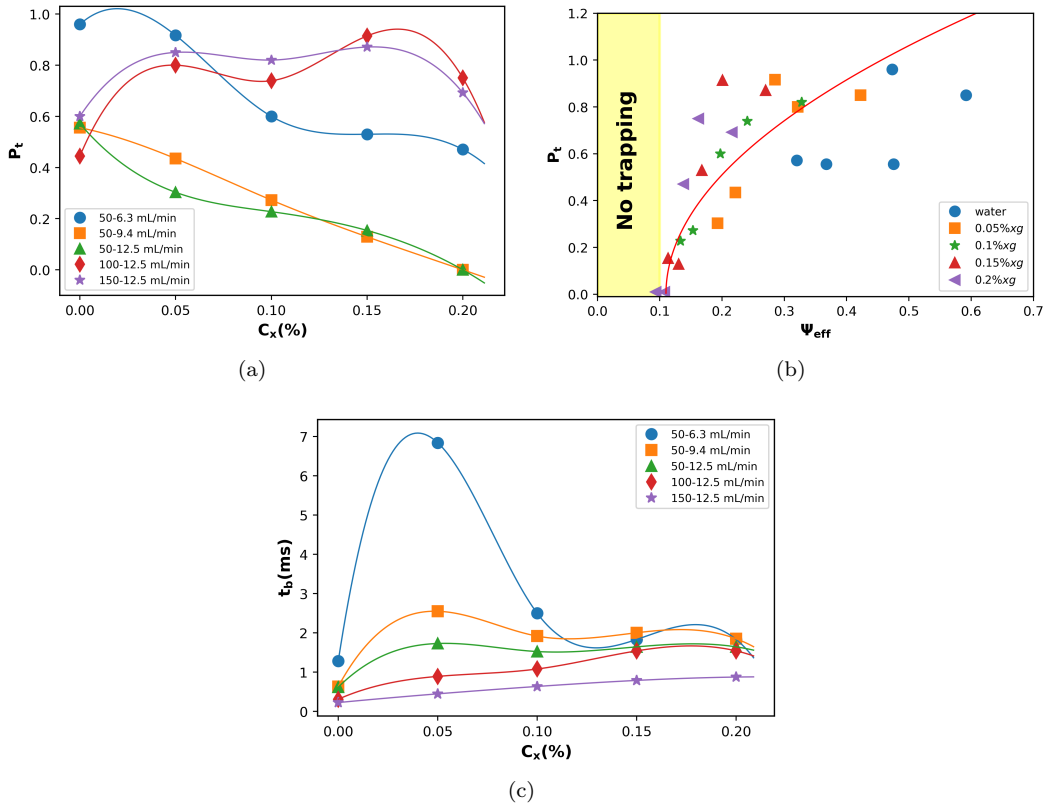


FIG. 8: (a) Probability of trapping of a single oil drop as a function of the concentration  $C_x$  of xanthan in the continuous phase for several combinations of flow rates indicated in the legend. The full lines are cubic spline interpolating functions that solely serve as a guide for the eye. (b) Dependence of the trapping probability  $P_t$  on the effective swirl efficiency  $\Psi_{eff}$ . The full line is a guide for the eye,  $P_t \propto (\Psi_{eff} - 0.1)^{0.5}$ . (c) Dependence of the averaged (over 100 individual events) breakup times of the single oil droplet for various flow rates indicated in the insert on the volume fraction of xanthan in the continuous phase. The full lines are cubic spline interpolating functions that solely serve as a guide for the eye.

triangles). As previously mentioned for other physical quantities we assessed through the paper, the location of this peak rather close to the overlap concentration  $C^*$  highlighted in Fig. 2(b). As the flow rates are gradually increased the peak flattens and, for the largest flow rates the dependence becomes monotonically increasing (the diamonds and the stars).

To get further understanding of the rather non-trivial dependence of the statistically averaged breakup times on the flow rates and xanthan concentration illustrated in Fig. 8(c), we focus in the following on a systematic description of the dynamics of the interfaces between the two fluids and the flow kinematics responsible for the drop breakup process.

A panorama of micro-graphs illustrating the single droplet dynamics and breakup observed at low flow rates ( $50 - 6.3 \text{ mL/min}$ ) for various xanthan concentrations is shown in Fig. 9. The time

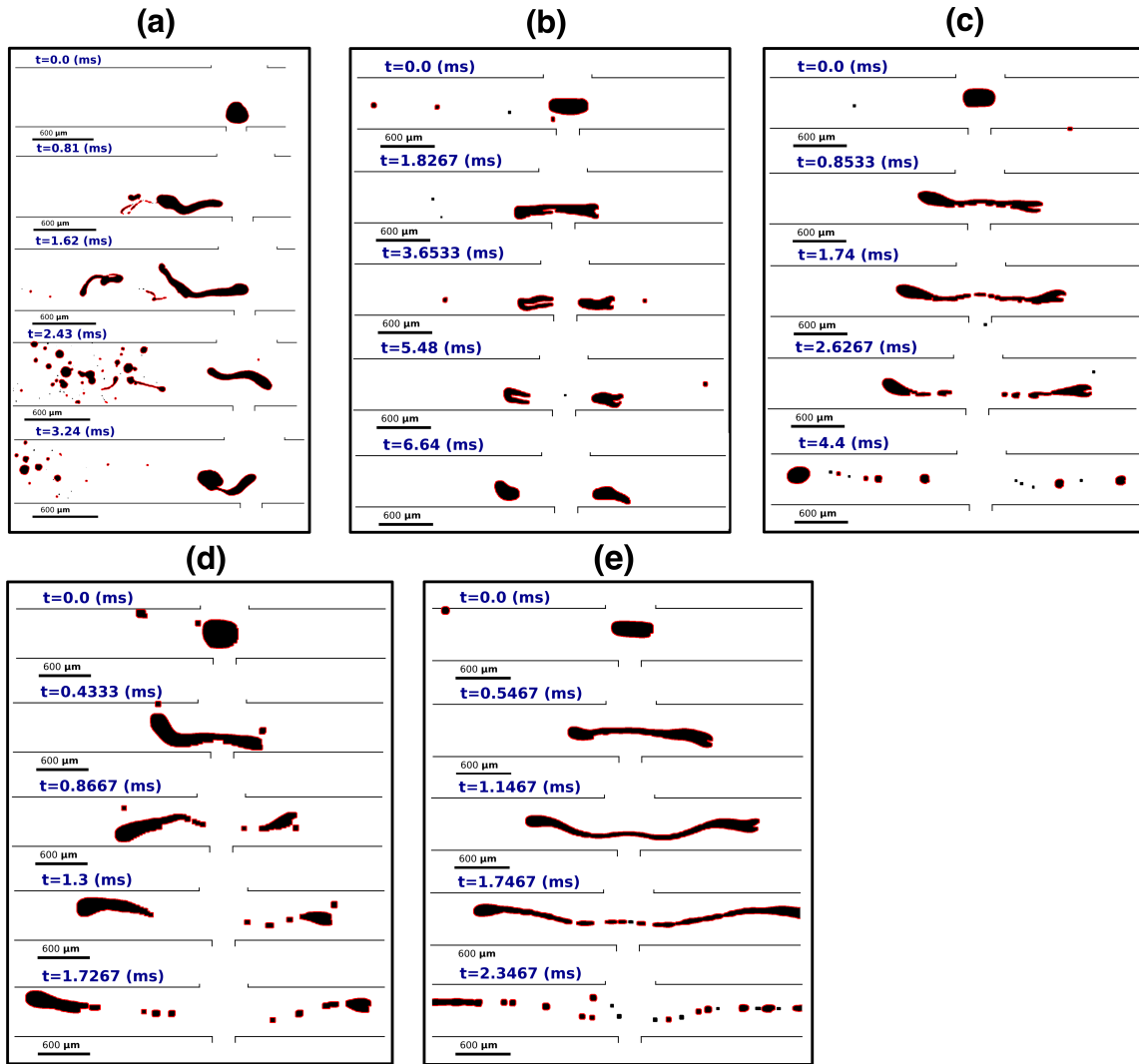


FIG. 9: Illustration of the dynamics of droplet breakup for several xanthan concentrations in the continuous phase and the flow rates  $50 - 6.3 \text{ mL/min}$ : (a)  $C_x = 0\%$ , (b)  $C_x = 0.05\%$ , (c)  $C_x = 0.1\%$ , (d)  $C_x = 0.15\%$ , (e)  $C_x = 0.2\%$ . In each sub-panel the red contours delineate the oil-water interface.

instants are indicated in the top inserts of each micro-graph.

A panorama of micro-graphs illustrating the single droplet dynamics and breakup observed at high flow rates ( $150 - 12.5 \text{ mL/min}$ ) for various xanthan concentrations is shown in Fig. 10.

We present in Fig. 11 the time dependence of the total number of daughter droplets (or filaments) observed in the field of view. Different symbols refer to the xanthan concentrations indicated in the inserts of each panel. The low speed breakup case ( $50 - 6.3 \text{ mL/min}$ ) visually illustrated in Fig. 9

is presented in panel 11(a) while the high speed case visually illustrated in Fig. 10 is presented in Fig. 11(b).

At short times, the number of droplets is of order of unity. This corresponds to mainly a single large mother drop entering the impingement flow region and, occasionally, several other much smaller droplets observed in the field of view. Our analysis solely focuses on the dynamics of the mother drop. After a characteristic time  $t_b$  the initial mother droplet undergoes a primary breakup triggered by the turbulent flow field surrounding it. The characteristic time  $t_b$  for the primary breakup to occur depends on both the xanthan concentration and the flow rates which mainly control the strength of the swirling motion and, consequently, the strength of the turbulent flow. The primary breakup of the initial mother drop is followed by deformation of the resulting drops and subsequent breakup events. Consequently, for  $t \geq t_b$ , the number  $N_{max}$  of objects (daughter droplets, filaments) detected in the field of view generally increases monotonically with time expect following a power-law.

For both flow rates investigated, the steepest increase of the number of objects is observed when water is used as a continuous phase. In the presence of xanthan, the breakup process is slower which is due to the presence of filaments.

A key element for the characterization of the dynamics of the drop breakup process relates to a statistical analysis of the morphology of the connected objects resulting from the breakup process.

To describe the morphology of the connected objects emerging upon the breakup of the mother drop we focus on the statistics of the sphericity of the daughter droplets observed in the field of view. For each droplet, we define a non dimensional sphericity parameter as:

$$\xi = \frac{4\pi A}{P^2} \quad (12)$$

where  $A$  is the area of the droplet (or filament) and  $P$  its perimeter.

This additional non-dimensional parameter characterizing the droplet shape is somewhat similar to the deformation parameter  $DP$  previously defined through the paper but, as it directly involves the areas and the perimeters of the detected droplets (rather just the main semi-axis of the deformed droplet object), it is probably more appropriate for telling the difference between quasi-spherical drops and filaments. Thus, for nearly spherical droplets,  $\xi \rightarrow 1$  while for filament-shaped droplets that are characterized by small areas and large perimeters,  $\xi \rightarrow 0$ . Probability density functions (pdf's) of the sphericity parameter at various xanthan concentrations are summarized in Fig. 12.

For the low flow rates case the pdf's gradually become doubly peaked as the xanthan concentration is gradually increased, Fig. 12(a). This doubly peaked behaviour of the pdf's relates to the coexistence of drops and filaments observed in Fig. 9.

A different shape and trend of the pdf's is observed for the high flow rates, Fig. 12(b). As the xanthan concentration is increased, the initial peak located near  $\xi \approx 1$  related to the presence of drops broadens significantly within the region  $\xi \in [0, 1]$  consistently with an increase of the number of low sphericity objects which are the long filaments observed in Fig. 10.

A key element in understanding the dynamics of the breakup phenomenon relates to assessing the flow structure around the drop. To do so, we employ the front tracking technique detailed in Sec. II C in order to assess the velocity distribution along the contour of the mother drop and, subsequently, the kinematics of its deformation. We illustrate in Fig. 13 contour speeds of an oil drop (top row) undergoing breakup in water for a combination of flow rates  $50 - 6.3 mL/min$  computed at several time instants indicated in the top inserts. Together with this, we illustrate on the bottom row of Fig. 13 the corresponding pdf's of the flow type parameter  $\lambda$  defined by Eq. 7.

Right after entering the impingement region ( $t = 0.34 ms$ ), the drop experiences both shear and extension. At later times the extensional part of the flow increases gradually though the flow

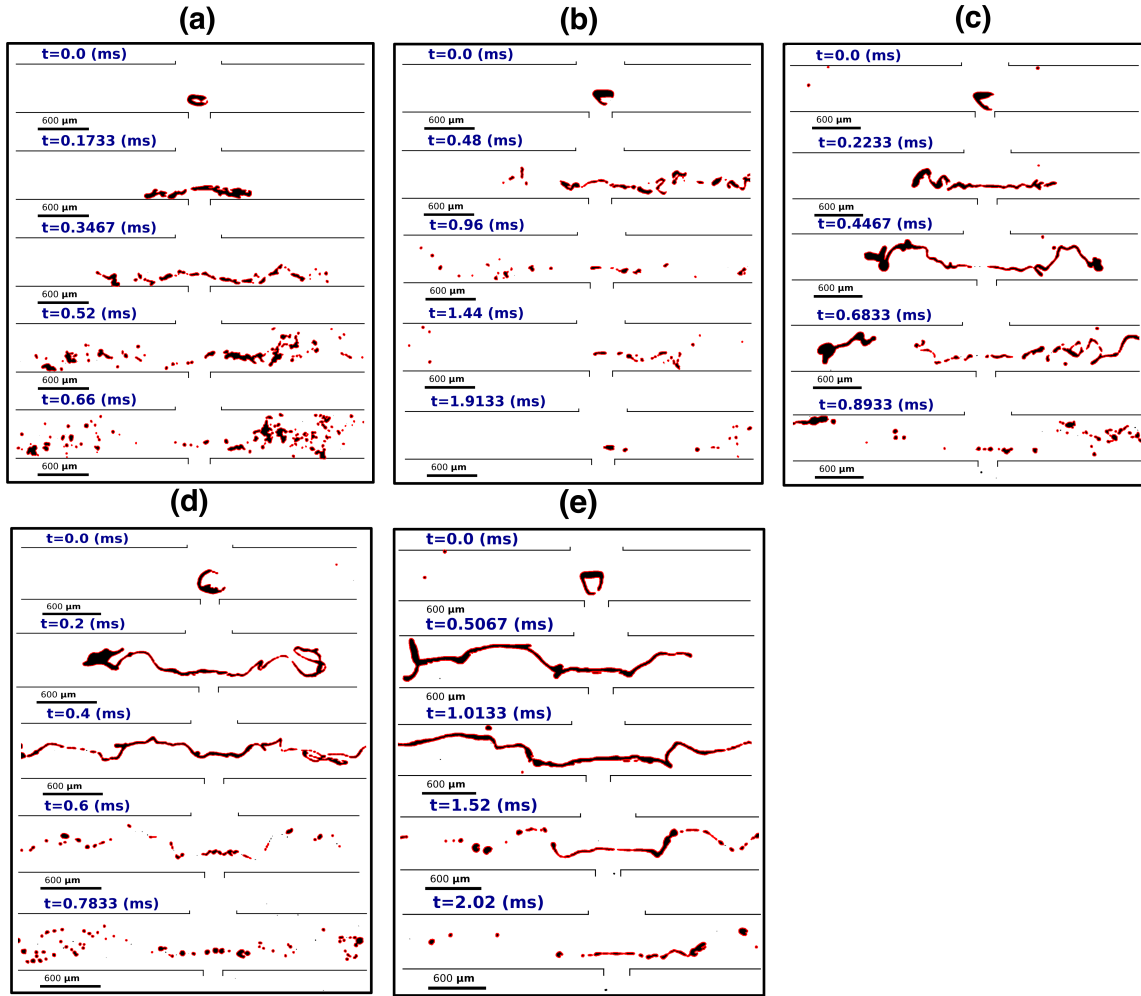


FIG. 10: Illustration of the dynamics of droplet breakup for several xanthan concentrations in the continuous phase and the flow rates  $150 - 12.5 \text{ mL/min}$ : (a)  $C_x = 0\%$ , (b)  $C_x = 0.05\%$ , (c)  $C_x = 0.1\%$ , (d)  $C_x = 0.15\%$ , (e)  $C_x = 0.2\%$ . In each sub-panel the red contours delineate the oil-water interface.

remains of mixed type. Close to the breakup ( $t = 2.42 \text{ ms}$ ) when a significant pinching effect is observed the flow field around the drop contour is extension dominated.

We illustrate in Fig. 14 time series of the total rate of deformation  $D_2$ , the extensional rate deformation  $\dot{\epsilon}$  and the rate of the shear deformation  $\dot{\gamma}$  computed from measurements of the contour velocity field exemplified in Fig. 13. The measurements were performed with water as a continuous phase and a combination of flow rates  $50 - 6.3 \text{ mL/min}$ . On the top row of the plot three distinct micro-graphs of the oil droplet corresponding to the time instants highlighted by full red circles in the main plot are presented.

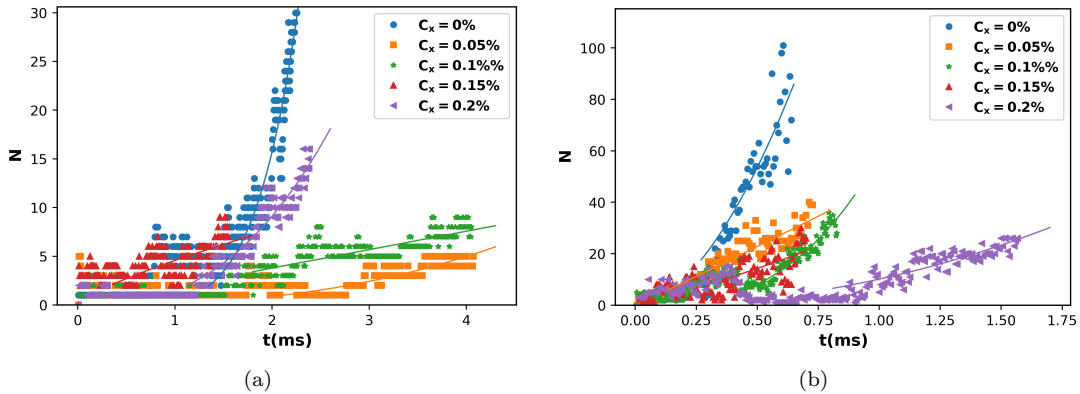


FIG. 11: Temporal evolution of the number  $N$  of connected objects (daughter droplets and filaments) observed in the field of view after the breakup of the single oil droplet for various concentrations of xanthan in the continuous phase indicated in the two inserts and two distinct choices of flow rates: (a) -  $50 - 6.3\text{mL}/\text{min}$  (b) -  $150 - 12.5\text{mL}/\text{min}$ . The full lines in each panel are power law fitting functions.

The spikes of the time series illustrated in Fig. 14 correspond to the the pinch off of the mother drop which precludes a breakup event.

We present in Fig. 15 the dependence of the rates of deformation (shear - empty symbols, extension - flow symbols) averaged in time until the primary breakup occurs ( $t < t_b$ ) on the xanthan concentration for two flow rates:  $50 - 6.3\text{mL}/\text{min}$  - circles,  $150 - 12.5\text{mL}/\text{min}$  - squares.

These measurements offer a second confirmation that the dynamics of the droplet is extension dominated and this is the case regardless the flow rates and xanthan concentrations.

It is rather clear at this point that in order to fully connect the single drop dynamics with the rheological behaviour of the fluid, measurements of the extensional viscosity are needed. Unfortunately, we are not aware of any technique able to assess the extensional viscosity at such high rates of extension. Through the reminder of the analysis we solely focus on the extensional part of the deformation field.

Based on simultaneous measurements of the time series of the characteristic size of the drop  $R(t)$  (estimated using the area  $A$  and perimeter  $P$  of the drop as  $R \approx \frac{2A}{P}$ ), the speed of its centroid  $V_C(t)$  and the extensional rate  $\dot{\epsilon}(t)$ , one can compute a time series of extensional deformations as  $\epsilon(t) = \frac{R(t)\dot{\epsilon}(t)}{V_C(t)}$ . The statistics of the extensional strains prior to the primary breakup of the mother drop ( $t < t_b$ ) are summarized in Fig. 16 for two combinations of flow rates:  $50 - 6.3\text{mL}/\text{min}$  - circles,  $150 - 12.5\text{mL}/\text{min}$  - squares.

For the lowest flow rates combination explored both the time averaged rate  $\langle \epsilon \rangle_{t < t_b}$  (Fig. 16(a)) and the root mean square (rms) of its fluctuations (Fig. 16(b)) are non-monotonical in xanthan concentration and exhibit a local maximum around  $C \approx C_x$ . For the highest flow rates combination both the time averaged extensional rate and the rms of its fluctuations are smaller than for the case of the smaller flow rates. It is important to note at this point that for both flow rates illustrated in Fig. 16 the rms of the fluctuations of the rate of extension is typically larger than its time averaged value which is consistent with the large values of the Reynolds number that render the primary swirling flow in the impingement region strongly turbulent.



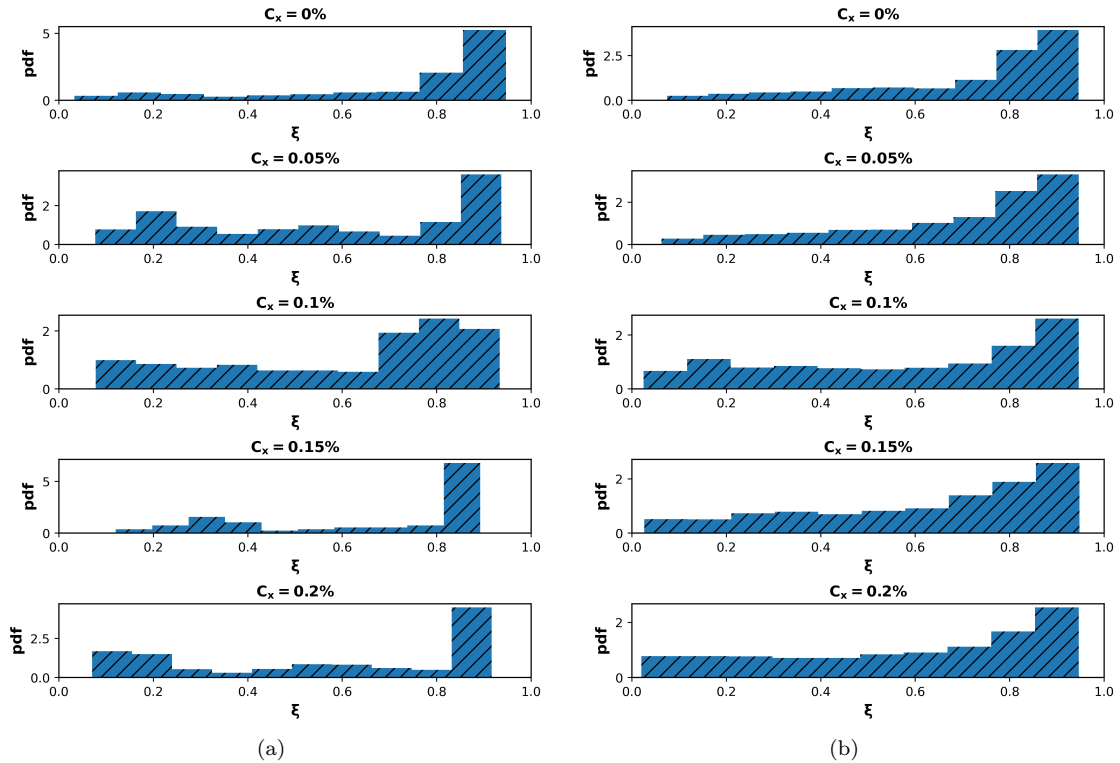


FIG. 12: Probability distributions of the sphericity parameter  $\xi$  of the oil droplets observed in the field of view for various xanthan concentrations in the continuous phase indicated in the top inserts and two combinations of flow rates: (a)  $50 - 6.3 \text{ mL/min}$  (b)  $150 - 12.5 \text{ mL/min}$ .

We summarize in Fig. 17 the various dynamic modes of a single oil droplet observed for various xanthan concentrations and various combinations of flow rates as a function of the effective swirl efficiency parameter  $\Psi_{eff}$  and the Reynolds number. The two fundamental dynamic modes discussed in Secs. III B and III C are mode *C* - trapping and no breakup (right triangles) and mode *B* - no trapping, breakup (squares). By exploring a wide range of flow rates and several xanthan concentrations, two additional dynamic modes that are combinations of the first two are observed: mode *A* - no trapping, no breakup and (the circles) mode *D* - trapping breakup (the left triangles). Corresponding to low values of the Reynolds numbers, only the modes *A* and *C* are observed. Upon a gradual increase of the Reynolds number and of the swirl efficiency parameter, the modes *B* and *D* start to develop. Corresponding to the highest values of the Reynolds number explored, only mode *D* is observed.

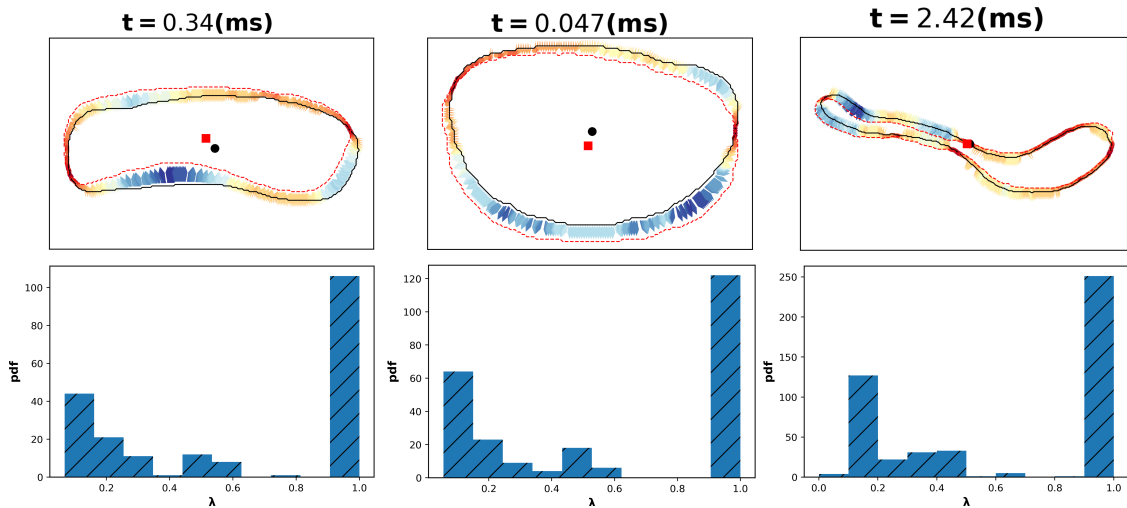


FIG. 13: **Top row:** Illustration of the front tracking (see Sec. II C for the technical details of the analysis) for a mother droplet in a water matrix and the flow rates  $50 - 6.3mL/min$  at several time instants indicated in the top inserts. The black full line represents the initial contour of the drop, the dashed red its final contour. The black circle is the initial centroid of the drop while the red square is its final centroid. The color map of the velocity vectors relates to their magnitude (red - small values, blue - large values). **Bottom row:** Corresponding probability density functions (pdf's) of the flow type parameter  $\lambda$  computed according to Eq. 7.

#### IV. CONCLUSIONS, OUTLOOK

A systematic experimental investigation of the dynamics of a Newtonian droplet (oil) in the turbulent cross-slot flow of xanthan solutions with various concentrations is presented.

The key physical processes underlying the emulsification in turbulent flow are the transient droplet deformation and, ultimately, its breakup. The present study brings insights into the role of shear thinning rheological behaviour on each of these two processes which may prove instrumental in understanding the dynamically more complex process of emulsification of shear thinning fluids in turbulent flows.

Two distinct phenomena have been studied by means of in-situ visualisation and a bespoke image processing protocol developed in house. The first one relates to the trapping of the mother droplet within the impingement region of the flow in the absence of breakup, Sec. III B. The swirl generated by the uneven sizes of the flow inlets within the impingement region translates into low pressures within the impingement region which lead to the drop trapping phenomenon.

Within these states the droplet does deform to a certain extent both while being trapped in the impingement zone and after escaping it but it does not breakup. Both the trajectories and the histories of their deformation depend on the concentration of xanthan in the continuous phase, Fig. 6. The main statistics of the trapping events are summarized in Fig. 7 in terms of both the drop deformation parameter  $DP$  and trapping time  $t_{trapping}$  for several concentrations of xanthan in the continuous phase. The central result relates to a monotonic increase of the trapping time when the xanthan concentration is gradually increased. Together with this, longer the drops stay trapped, larger their time averaged deformation  $\langle DP \rangle_t$  is. The statistics of the drop velocity do not

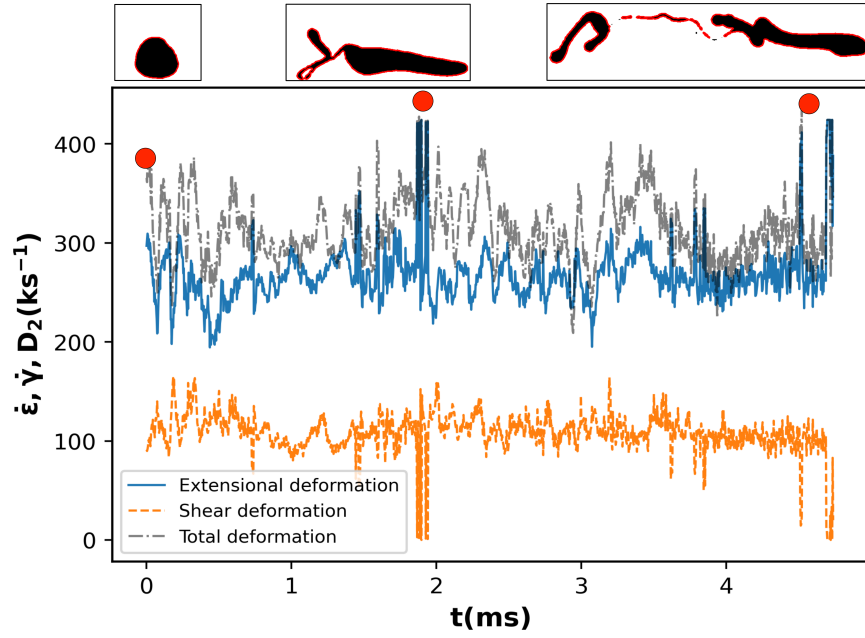


FIG. 14: Time series of the shear deformation  $\dot{\gamma}$  (dashed line), extensional deformation  $\dot{\epsilon}$  (full line) and total deformation  $D_2$  (dash-dotted line). The measurements were performed with water as a continuous phase and a combination of flow rates  $50 - 6.3 \text{ mL/min}$ . Micro-graphs of the mother drop acquired at the time instants marked by the full red circles in the main plot are illustrated on the top line.

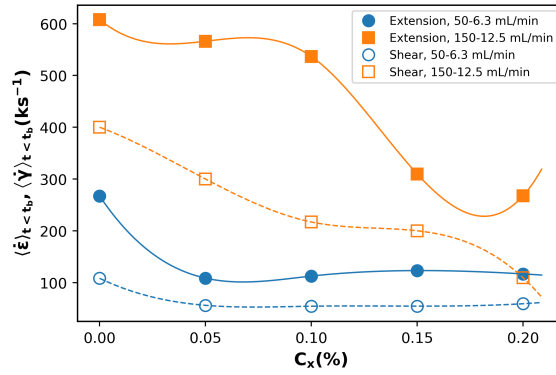


FIG. 15: Dependence of the time averaged rates of shear (open symbols) and extension (full symbols) averaged prior to the primary breakup of the mother drop on the xanthan concentration. The symbols refer to the combinations of flow rates indicated in the insert. The lines are cubic spline interpolating functions that serve as a guide for the eye.

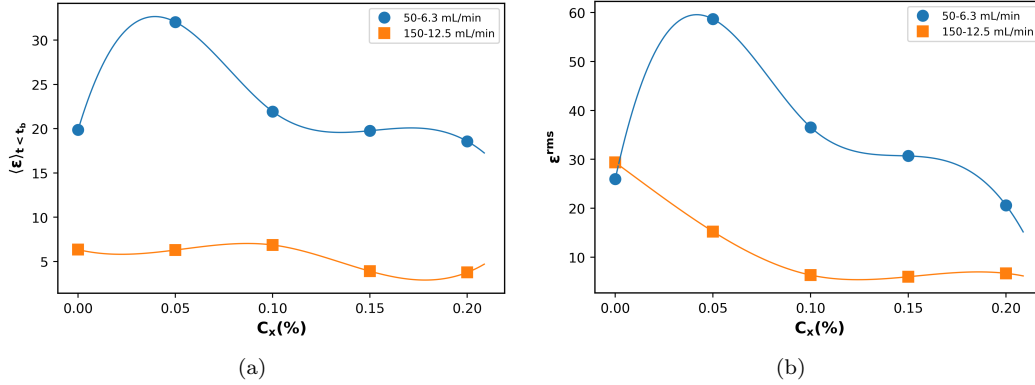


FIG. 16: Statistics of the extensional strains  $\epsilon$  prior to the primary breakup at various xanthan concentrations: (a) - time average, (b) - rms of fluctuations. In each panel the symbols refer to the combinations of flow rates indicated in the insert and the lines are cubic spline interpolating functions that serve as a guide for the eye.

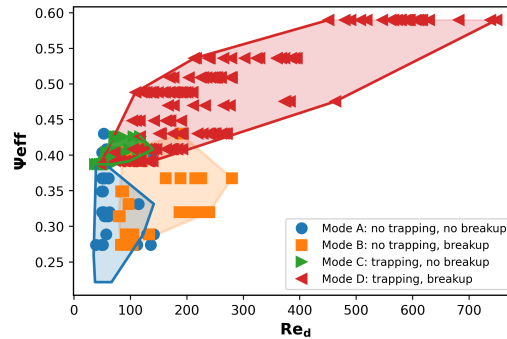


FIG. 17: Dynamic modes of single oil drop observed in both Newtonian and non-Newtonian fluid matrices. The four experimentally observed dynamic modes detailed in the manuscript are indicated in the legend.

follow a clear trend with the xanthan concentration, Fig. 7(d). Though we do not have a definite explanation for this we believe it may originate from either the three dimensionality of the flow (we only have access to the in-plane velocity) or the coupling between the flow kinematics and the shear thinning rheology of the continuous phase. The trend of the dependence of the trapping probability  $P_t$  with the xanthan is strongly influenced by the magnitude of the driving flow rates, Fig. 8(a). For low values of the flow rates, the trapping probability decreases monotonically with the xanthan concentration; while for higher flow rates the dependence becomes non-monotonic. This is a clear indicator that the trapping behaviour relates to both the flow conditions (the flow rates) and the shear thinning rheology of the continuous phase. This prompted us to define a non dimensional

parameter  $\Psi_{eff}$  that quantifies the effective strength of the swirling motion that dominates the impingement region by accounting for both the inlet flow conditions (flow rates) and the rheological behaviour, Eq. 10. Indeed, when plotted against this effective flow strength parameter, the trapping probabilities follow a common square root trend indicating that with respect to this control parameter the trapping events emerge via an imperfect bifurcation, Fig. 8(b).

A second phenomenon that is of paramount importance for understanding the process of emulsification relates to the breakup of drops, Sec. III C. The characteristic breakup times depend on both the flow rates and the rheology of the continuous phase, Fig. 8(c). For low flow rates, the dependence of the breakup time on the xanthan concentration is non-monotonic exhibiting a peak around the overlap concentration  $C^*$ . For higher flow rates a monotonic dependency of the breakup time on the xanthan concentration is observed: larger the concentration is, longer it takes for the mother drop to break. The intricate coupling between the breakup dynamics, flow conditions and rheology of the continuous phase prompted us to resort to a systematic analysis of the drop morphology, Figs. 9, 10. The breakup of the mother drops yields two morphological distinct connected objects: daughter drops and filaments.

The time dependence of the number of connected objects observed in the field of view is summarized in Fig. 11 for two combinations of flow rates and several xanthan concentrations in the continuous phase. After the primary breakup of the mother drop, the number of connected objects increases as a power law with time. The rate of this increase depends on both the flow rates and the concentration of xanthan. For both combinations of flow rates illustrated in Fig. 11 the steepest increase of the number of connected objects is observed when pure water is used as a continuous phase. As the concentration of xanthan is gradually increased, the rate of increase of number of connected objects decreases indicating that the shear thinning rheology of the continuous phase inhibits the dynamics of the successive breakup events.

To distinguish between the connected objects emerging upon the breakup of a mother drop and provide a statistical picture of their emergence, we have computed for each object detected in the field of view a sphericity parameter  $\xi$  defined by Eq. 12. The statistics of the sphericity parameter are summarized in Fig. 12 for two combinations of flow rates and various concentrations of xanthan in the continuous phase. In the absence of xanthan in the continuous phase, the pdf's of the sphericity are peaked at large values,  $\xi \approx 0.85$  indicated that the drops represent the dominant morphology. At smaller flow rates, a gradual increase of the xanthan concentration renders the pdf's of the sphericity doubly peaked, Fig. 12(a). This corresponds to a co-existence of drops and filaments as visible in Fig. 9. The shape of the pdf's is substantially different at higher flow rates, Fig. 12(b). Upon an increase of the xanthan concentration the pdf's remain single peaked but a low  $\xi$  tail gradually develops indicating the progressive emergence of filaments which become now significantly long, Fig. 10.

Key insights into the breakup dynamics of a single drop entering the impingement region of the micro-channel may be obtained by a systematic description of the flow kinematics. Such description is classically achieved using the Particle Image Velocimetry technique, which can not be technically implemented here. Alternatively, a simple yet novel technique is proposed that allows one to compute the distribution of the velocity along the contour of the drop, Figs. 5(b), 13. The measurements of the contour velocity allows one to compute the second invariant of the rate of deformation tensor  $D_2$  according to Eq. 5. To distinguish between the shear and extensional part of the drop deformation, we subsequently compute the flow type parameter  $\lambda$  according to Eq. 7. An important conclusion drawn from the measurements of the flow parameter is that the deformation of the drop encompasses both shear and extension - see bottom row in Fig. 13. In terms of the magnitude of the rates of the deformation, however, the extension appears to be dominant, Fig. 14. At high flow rates, the averaged rates of deformation are more sensitive to the xanthan

concentration (and follow a decreasing trend) than at low flow rates, Fig. 15. The breakup process of the droplet depends on both the average rates of extension (or the capillary number) and the average deformation. This prompted us to perform a statistical analysis of the extensional deformations, Fig. 16. For the lowest combination of flow rates investigated, the extensional deformations averaged in time until the primary breakup of mother drop was observed to follow a non-monotonic trend with the xanthan concentration which passes through a local maximum around  $C \approx C^*$ , the circles Fig. 16(a). This non monotonic dependence is very similar in shape with the dependence of the breakup times on the concentration, Fig. 8(c). For the highest combination of the flow rates explored, the averaged strains are less sensitive to the xanthan concentration, the squares in Fig. 16(a). Quite interestingly, the averaged values of the extensional strains measured at high flow rates are smaller than those measured at lower flow rates. The turbulent microscopic flow that leads to the successive breakup events is characterized by strong fluctuations of both the rates of deformation, Fig. 14 and of the time averaged extensional strains Fig. 16(b). The dynamic modes associated to the droplet trapping and breakup depend on both the values of the effective swirl parameter  $\Psi_{eff}$  and the Reynolds number of the mother drop, Fig. 17.

The relevance of the present study is two-fold. First, along a fundamental line, our this study provides valuable insights into the role of shear thinning rheological behaviour on both the transient deformation of droplets and their subsequent breakup in a turbulent flow. As already stated through the paper, we believe these insights might prove instrumental in understanding the dynamically more complex problem of microscopic scale emulsification.

Along a more applied and technical line, our study proposes a novel state of art technique of assessing the flow fields along the contour of the drops based on a front tracking algorithm. This method which complements the classical micro-*PIV* technique is rather straightforward to implement as it solely requires sharp images of the drops and ultimately provides a full kinematic description of the flow field responsible for the droplet deformation and its subsequent breakup.

Our experimental observations prompt for several aspects to be dealt with in future studies. First, it would be interesting to implement microscopic *PIV* measurements and quantitatively assess the space-time dynamics of the flow fields. Our study has clearly demonstrated that the primary breakup of the oil drop is mainly driven by the strong extensional component, Fig. 14, 15. As it would be interesting at this point to understand the scaling of the critical capillary number at breakup (defined using a scale for the rates of extension) with the control parameter,  $\Psi_{eff}$ . This calls for new developments in extensional rheology at rates comparable in magnitude to the ones we report.

## V. ACKNOWLEDGEMENTS

We gratefully acknowledge the "Region Pays de la Loire" for funding the project *Connect Talent ODE "Optical Diagnostics for Energy"*.

- 
- [1] Agarwal, V. G., R. Singh, S. S. Bahga, and A. Gupta (2020), *Phys. Rev. Fluids* **5**, 044203.
  - [2] Belkadi, A., D. Tarlet, A. Montillet, J. Bellettre, and P. Massoli (2015), *International Journal of Multiphase Flow* **72**, 11.
  - [3] Burghelca, T., and V. Bertola (2019), *Transport phenomena in complex fluids* (Springer International Publishing).
  - [4] Callen, H. (1985), *Thermodynamics and an introduction to thermostatistics* (Wiley, New York).

- [5] Chiarello, E., L. Derzsi, M. Pierno, G. Mistura, and E. Piccin (2015), *Micromachines* **6** (12), 1825.
- [6] Chiarello, E., A. Gupta, G. Mistura, M. Sbragaglia, and M. Pierno (2017), *Phys. Rev. Fluids* **2**, 123602.
- [7] Derzsi, L., M. Kasprzyk, J. P. Plog, and P. Garstecki (2013), *Physics of Fluids* **25** (9), 092001, <https://doi.org/10.1063/1.4817995>.
- [8] Fardin, M. A., M. Hautefeuille, and V. Sharma (2022), *Soft Matter* **18**, 3291.
- [9] Fragkopoulos, A. A., E. Pairam, L. Marinkovic, and A. Fernández-Nieves (2018), *Phys. Rev. E* **97**, 021101.
- [10] Fu, T., Y. Ma, and H. Z. Li (2016), *Chemical Engineering Science* **144**, 75.
- [11] Fuller, G., and L. Leal (1981), *Journal of Non-Newtonian Fluid Mechanics* **8** (3), 271.
- [12] Guido, S., M. Simeone, and F. Greco (2003), *Polymer* **44** (2), 467.
- [13] Guillot, P., P. Panizza, J.-B. Salmon, M. Joanicot, A. Colin, C.-H. Bruneau, and T. Colin (2006), *Langmuir* **22** (14), 6438, pMID: 16800711, <https://doi.org/10.1021/la060131z>.
- [14] Gupta, A., and M. Sbragaglia (2016), *The European Physical Journal E* **39** (1), 2.
- [15] Ji, Y., J. Bellettre, A. Montillet, and P. Massoli (2020), *International Journal of Multiphase Flow* **131**, 103402.
- [16] Ji, Y., J. Bellettre, A. Montillet, and P. Massoli (2021), *Experiments in Fluids* **62** (1), 17.
- [17] Kilpatrick, P. K. (2012), *Energy & Fuels* **26** (7), 4017, <https://doi.org/10.1021/ef3003262>.
- [18] Landau, L. D., and E. M. Lifshits (1980), *Statistical Physics, Part 1: Volume 5 (Course of Theoretical Physics, Volume 5)*, third edition ed. (Butterworth-Heinemann).
- [19] Lopes, R., R. O. Rodrigues, D. Pinho, V. Garcia, H. Schütte, R. Lima, and S. Gassmann (2015), in *2015 IEEE International Conference on Industrial Technology (ICIT)*, pp. 3347–3350.
- [20] Macosko, C. W. (1994), *Rheology: principles, measurements, and applications* (Wiley, New York).
- [21] McClements, D. J. (2005), “Food emulsions: principles, practices, and techniques. 2. ed.” (Boca Raton, Fla.: CRC Press;) p. 609.
- [22] Miller, C. (1972), *Industrial & Engineering Chemistry Fundamentals* **11** (4), 524, <https://doi.org/10.1021/i160044a015>.
- [23] Montillet, A., S. Nedjar, and M. Tazerout (2013), *Fuel* **106**, 410.
- [24] Nehme, R., W. Blel, A. Montillet, J. Bellettre, and L. Marchal (2021), *Chemical Engineering and Processing - Process Intensification* **161**, 108301.
- [25] Nghe, P., E. Terriac, M. Schneider, Z. Z. Li, M. Cloitre, B. Abecassis, and P. Tabeling (2011), *Lab Chip* **11**, 788.
- [26] Nooranidoost, M., D. Izbassarov, and M. Muradoglu (2016), *Physics of Fluids* **28** (12), 123102, <https://aip.scitation.org/doi/pdf/10.1063/1.4971841>.
- [27] Nsengiyumva, E. M., and P. Alexandridis (2022), *International Journal of Biological Macromolecules* **216**, 583.
- [28] Pipe, C. J., T. S. Majmudar, and G. H. McKinley (2008), *Rheologica Acta* **47** (5), 621.
- [29] Ren, Y., Z. Liu, and H. C. Shum (2015), *Lab Chip* **15**, 121.
- [30] Rodd, A., D. Dunstan, and D. Boger (2000), *Carbohydrate Polymers* **42** (2), 159.
- [31] Roy, A. (2015), *Synthèse et caractérisation de dérivés amphiphiles du xanthane*, Ph.D. thesis (Université du Havre).
- [32] Sepulveda, J., A. Montillet, D. D. Valle, T. Amiar, H. Ranchon, C. Loisel, and A. Riaublanc (2021), *Applied Rheology* **31** (1), 24.
- [33] Sworn, G. (2009), “Handbook of hydrocolloids,” Chap. Xanthan gum (Boca Raton, Fla.) pp. 186–203.
- [34] Taylor, G. I. (1934), *Proceedings of the Royal Society of London. Series A, Containing Papers of a Mathematical and Physical Character* **146** (858), 501, <https://royalsocietypublishing.org/doi/pdf/10.1098/rspa.1934.0169>.
- [35] Thorsen, T., S. J. Maerkl, and S. R. Quake (2002), *Science* **298** (5593), 580, <https://www.science.org/doi/pdf/10.1126/science.1076996>.
- [36] Tretheway, D. C., and L. Leal (2001), *Journal of Non-Newtonian Fluid Mechanics* **99** (2), 81.
- [37] Van Aken, G. (2009), “Food polysaccharides and their applications. 2nd ed.” Chap. Food science and technology (Boca Raton, FL: CRC/Taylor & Francis) p. 521–539.
- [38] van der Walt, S., J. L. Schönberger, J. Nunez-Iglesias, F. Boulogne, J. D. Warner, N. Yager, E. Gouillart, T. Yu, and the scikit-image contributors (2014), *PeerJ* **2**, e453.

- [39] Zhao, C.-X., and A. P. Middelberg (2011), *Chemical Engineering Science* **66** (7), 1394, microfluidic Engineering.
- [40] Zhou, H., C. Zhu, T. Fu, Y. Ma, and H. Z. Li (2019), *Chemical Engineering Science* **208**, 115158.